

IR Dust Bubbles: Probing the Detailed Structure and Young Massive Stellar Populations of Galactic HII Regions

C. Watson¹, M.S. Povich², E.B. Churchwell², B.L. Babler², G. Chunev¹, M. Hoare⁵, R. Indebetouw³, M.R. Meade², T.P. Robitaille⁶, B.A. Whitney⁴

ABSTRACT

We present an analysis of wind-blown, parsec-sized, mid-infrared bubbles and associated star-formation using GLIMPSE/IRAC, MIPS GAL/MIPS and MAG-PIS/VLA surveys. Three bubbles from the Churchwell et al. (2006) catalog were selected. The relative distribution of the ionized gas (based on 20 cm emission), PAH emission (based on 8 μm , 5.8 μm and lack of 4.5 μm emission) and hot dust (24 μm emission) are compared. At the center of each bubble there is a region containing ionized gas and hot dust, surrounded by PAHs. We identify the likely source(s) of the stellar wind and ionizing flux producing each bubble based upon SED fitting to numerical hot stellar photosphere models. Candidate YSOs are also identified using SED fitting, including several sites of possible triggered star formation.

Subject headings: HII regions — ISM: bubbles — infrared: ISM — radio continuum: ISM — stars: formation

1. Introduction

Mid-infrared (MIR) imaging surveys of the Galactic plane such as the Mid-Course Space Experiment (MSX; Price et al. 2001) and the Galactic Legacy Infrared Midplane Survey

¹Manchester College, Dept. of Physics, 604 E. College Ave., North Manchester, IN 46962

²Univ. of Wisconsin - Madison, Dept. of Astronomy, 475 N. Charter St., Madison, WI 53716

³Department of Astronomy, University of Virginia, P.O. Box 3818, Charlottesville, VA 22903-0818

⁴University of Colorado, Space Science Institute, 1540 30th St., Suite 23, Boulder, CO 80303-1012

⁵School of Physics and Astronomy, University of Leeds, Leeds, West Yorkshire, LS2, 9JT

⁶SUPA, School of Physics and Astronomy, University of St Andrews, North Haugh, KY16 9SS, St Andrews, United Kingdom

Extraordinaire (GLIMPSE; Churchwell et al. 2001; Benjamin et al. 2003) have revealed a large number of bubbles in the disk of the Galaxy. The bubbles have bright $8\ \mu\text{m}$ shells that enclose bright $24\ \mu\text{m}$ interiors. ISO (Infrared Space Observatory; Kessler et al. 1996) and MSX were the first to reveal the existence of these objects (including the association with triggered star-formation, Deharveng et al. 2005), but the GLIMPSE survey (with ten times better spatial resolution and a hundred times the sensitivity than MSX) has enabled the detection of many more bubbles and has enabled the refinement of their morphological structure. In fact, the GLIMPSE survey has shown that bubbles are a hallmark of the diffuse emission in the Galactic plane. Small and faint bubbles are apparent only in the GLIMPSE survey due to the lower resolution and sensitivity of MSX. Churchwell et al. (2006; 2007) have cataloged almost 600 bubbles. An average of $\gtrsim 5$ bubbles per square degree were found within 20° of the Galactic center. These bubbles are identified as complete or partial rings in the GLIMPSE images, which Churchwell et al. (2006) argue are two dimensional representations of three dimensional bubbles. Churchwell et al. (2006) showed that the bubbles are distributed in longitude and latitude like O and B stars, $>25\%$ of which are coincident with known radio HII regions, and $\sim 13\%$ enclose known stellar clusters. About $1/3$ of the bubbles are produced by O stars. Approximately two thirds of the sample have small angular diameters, which Churchwell et al. (2006) propose to be mostly physically small bubbles produced by late B type stars whose UV photon fluxes are adequate to excite a shell of PAH emission but not adequate to produce a detectable radio HII region. Churchwell et al. (2006; 2007) tabulated bubble morphological properties such as angular diameter, shell thickness, and eccentricity.

Bubbles/HII regions identified by MIR emission present a new and powerful tool to study the interaction of young hot stars with their environment. Young stars impact the ambient interstellar medium (ISM) by heating the dust, ionizing the gas (in the case of O and early B stars), and heating an expanding bubble. Bubbles can be produced by stellar winds and over-pressure by ionization and heating by stellar UV radiation. Bubble sizes and morphologies are determined by the density structure of the ambient ISM, the luminosity of the central star(s) responsible for producing the bubble, the stellar wind luminosity and the motion of the central star(s) relative to the ambient ISM. The morphologies of MIR dust bubbles/HII regions reveal important information about the strength and directionalities of stellar winds and the structure and physical properties of the ambient ISM into which the bubbles are expanding. Pillars, scalloping, and sharpness of the inner boundaries of bubbles defined by $8\ \mu\text{m}$ emission provide unique insights into the hydrodynamics, photo-ionization, and evaporation of gas and sublimation of dust in expanding bubbles, and stellar mass loss rates during their evolution. For example, based on GLIMPSE-MIR morphology of ultra-compact (UC) HII regions, Hoare et al. (2007) and references therein have found

an unusually high fraction of cometary shapes. They argue that the morphology of the PAH-traced photo-dissociated region (PDR), combined with the radio free-free emission, is suggestive of a champagne flow.

MIR bubbles that surround HII regions ionized by O stars and B supergiants (i.e. those that have strong stellar winds) have been modeled by several groups. Analytic evolution models have been developed by Castro, McCray, and Weaver (1975), Weaver et al. (1977), Whitworth et al. (1994), and Capriotti and Kozminsky (2001). These models predict that wind-blown bubbles around O stars and B supergiants should have the following distinct regions: a hypersonic stellar-wind-evacuated central cavity surrounding the central star where densities are very low; a hot, low-density, shocked stellar wind region surrounding the central evacuated cavity that occupies most of the volume of the HII region; a thin conduction zone where temperature sharply decreases and density rapidly increases (with radius); a thin, dense shell of shocked H^+ gas surrounded by a very thin shell of non-shocked H^+ gas at about 10^4 K. The outer thin shell of 10^4 K H^+ gas is the region classically thought to represent the photo-ionized HII region. This basic picture is supported by detailed numerical evolution models calculated for a $35 M_{\odot}$ (Freyer, Hensler, & Yorke, 2006; hereafter FHY06), a $60 M_{\odot}$ (Freyer, Hensler, and Yorke, 2003), and an $85 M_{\odot}$ star (Kröger, Hensler, & Freyer, 2006, and Kröger, Freyer, Hensler, & Yorke, 2007). The numerical models, however, show that the sharp boundaries predicted by the analytic models probably are not sharp due to turbulent mixing. The consequence of this is that clumps of cool 10^4 K gas are predicted to be found mixed with the hot 10^7 K gas. The thickness of the 10^4 K shell is predicted to be a function both of age and luminosity of the central star; the lower the wind luminosity the thicker the cool ionized shell is. Also the outer boundaries of the HII regions are predicted to be quite jagged due to instabilities produced when a dense medium expands into a much lower density interstellar medium (ISM). We will compare some of the model predictions with our observations in §5. All theoretical evolution models up to now have omitted the possible role of dust in HII regions, which new MIR observations clearly demonstrate is present.

Recent observations are providing a deeper understanding of the relative distributions of thermal dust, PAHs, ionized gas, and PDRs. Peeters et al. (2005) review the ISO spectroscopic observations of compact and evolved HII regions and the PDRs surrounding them. They find gas temperatures in the PDRs between 100 K (NGC 2024) and 200 K - 500 K (S106IR) and densities between 10^4 cm^{-3} (W75N) and 10^6 cm^{-3} (NGC 2024). They find broad agreement between these results and models of the illumination of PDRs by the appropriate nearby hot star(s). Kassis et al. (2006), on the other hand, report ground-based observations of the Orion bar that indicate PAHs are present just outside the HII region. They show that $[\text{Ne II}] 12.81 \mu\text{m}$ emission traces the geometry of the PDR in the bar. They also conclude that there is not a sharp transition between neutral and ionized PAH emission

within the PDR.

Each of the four Spitzer/IRAC (Infrared Array Camera) bandpasses are dominated by different emission processes in the neighborhood of a hot star (see Draine 2003 and Peeters et al. 2003). The brightest objects in the $3.6\mu\text{m}$ band are stars, but this band also has contributions from a weak, diffuse PAH feature at $3.3\mu\text{m}$, and possibly from scattered star light. The $4.5\mu\text{m}$ band samples diffuse emission in the $\text{Br}\alpha$ and $\text{Pf}\beta$ lines (from HII regions), H_2 $v=0-0$, S(9), S(10), and S(11) and CO $v=1-0$ ro-vib lines at $4.665\mu\text{m}$ (from shocked molecular gas). The $4.5\mu\text{m}$ band contains no PAH features and the brightest sources in this band are also stars. The $5.8\mu\text{m}$ band contains a strong PAH feature at $6.2\mu\text{m}$ which can dominate the diffuse emission except very close to O stars where PAHs are destroyed (see §4.1). Near hot O stars, strong contributions from thermally emitting dust plus a small contribution from stochastically heated small grains probably dominate the diffuse emission in the $5.8\mu\text{m}$ band. The $8.0\mu\text{m}$ band contains two very strong PAH features at 7.7 and $8.6\mu\text{m}$ which dominate the diffuse emission in this band, although near hot stars it may be dominated by thermal dust emission with little or no PAH emission. Within ionized zones, Hoare (1990) and Hoare et al. (1991) have shown that trapped Lyman α heated dust can maintain $T > 100$ K throughout the ionized region. Because the emission process that dominates in each IRAC band depends on the environment, band ratios provide a powerful tool to measure the extent of each environment.

The main focus of this study is to use wavelength-dependent distributions of MIR diffuse dust emission and high resolution radio continuum emission to determine the PAH destruction radius of three bubbles and to trace the relative sizes and locations of 1) the HII region, 2) the hot thermally emitting dust, and 3) the location and extent of the PDR region associated with each bubble. In section 2 we introduce the different data sets used for this analysis. In section 3, we discuss results of the observations toward three bubbles. In section 4, we estimate the PAH destruction radius and dust temperature. In section 5, we examine the stellar population within each of the bubbles to identify the ionizing star(s) and any young stellar objects (YSOs) associated with the bubbles. Conclusions are summarized in section 6.

2. Data

Data have been assembled from three imaging surveys of the galactic plane: GLIMPSE, MIPS GAL, and MAGPIS. The latter two surveys were chosen based on their resolution, sensitivity, wavelength coverage and overlap with the GLIMPSE survey which provided the basis for the Churchwell et al. (2006) bubble catalog. The GLIMPSE survey (Benjamin

et al. 2003) imaged the inner Galactic plane using the IRAC camera (Fazio et al. 2004) on the Spitzer Space Telescope (Werner et al. 2004). The survey covered $10^\circ < |l| < 65^\circ$ and $|b| < 1^\circ$ at $3.6 \mu\text{m}$, $4.5 \mu\text{m}$, $5.8 \mu\text{m}$ and $8.0 \mu\text{m}$ with resolution from $1.5''$ ($3.6 \mu\text{m}$) to $1.9''$ ($8.0 \mu\text{m}$). Mosaicked images were produced using the IPAC Montage program in the GLIMPSE pipeline after image artifacts were removed. A Point Source Archive was produced of all point sources detected above the 5σ level, about 48 million sources. See the GLIMPSE Data Products Description¹ for further details.

MIPSGAL (Carey et al. 2005) is a survey of the inner Galactic plane ($10^\circ < |l| < 65^\circ$ and $|b| < 1^\circ$) at $24 \mu\text{m}$ and $70 \mu\text{m}$ using the MIPS (Multiband Imaging Photometer for Spitzer) instrument (Rieke et al. 2004) on the Spitzer Space Telescope. MIPS has a resolution of $5''$ at $24 \mu\text{m}$ and $15''$ at $70 \mu\text{m}$. We only analyzed the $24 \mu\text{m}$ emission because the $70 \mu\text{m}$ appears complex enough to warrant separate analysis in an upcoming paper.

The Multi-Array Galactic Plane Imaging Survey (MAGPIS; Helfand et al. 2006) used the VLA in B, C and D configurations combined with the Effelsberg 100m single dish data to obtain high resolution radio images (with no zero spacing problems) at 1.4 GHz continuum. The survey covered $5^\circ < l < 32^\circ$ and $|b| < 0.8^\circ$ with a resolution of $6''$ and a 1σ sensitivity of ~ 0.3 mJy. Full polarization was preserved.

3. Results

We now present the relative distribution of MIR and 20 cm emission for three bubbles selected because they represent different morphological shapes and/or show possible evidence for triggered star formation. They are N10, N21 and N49 in the Churchwell et al. (2006) bubble catalog.

3.1. N10

N10 is a bright MIR and radio continuum bubble having elliptical or slight cometary shape with an opening at galactic position angle of 160° (see Fig. 1). Its kinematic distance is 4.9 ± 0.5 kpc (Churchwell et al. 2006 and references therein). At 1.4 GHz it has an integrated flux density of 7.58 Jy (Helfand et al 2006) and we measure an average angular radius to the

¹www.astro.wisc.edu/sirtf/glimpse1_dataprod_v2.0.pdf

background of 1.26' (~ 1.8 pc). Using the relation of (Rohlfs & Wilson, 2006):

$$\frac{N_{Ly}}{s^{-1}} = 6.3 \times 10^{52} \left(\frac{T_e}{10^4} \right) \left(\frac{\nu}{GHz} \right)^{-0.1} \left(\frac{L_\nu}{10^{20} WHz^{-1}} \right),$$

we calculate 1.6×10^{49} ionizing photons per second are necessary to maintain ionization, equivalent to a single O5V star (Martins, Schaerer & Hillier 2005, hereafter MSH05). No correction for extinction was made.

The relative distributions of emission as a function of wavelength are illustrated in Figs. 2-3. The bubble is surrounded by an $8\mu\text{m}$ emission shell with angular radius (out to the Galactic background level) of 1.8' (2.6 pc). The radius to the inner face of the $8\mu\text{m}$ shell is 1.2' (1.7 pc). The $8\mu\text{m}$ emission rises very sharply on the inner face of the shell and declines gradually with increasing radius. We postulate that this ring is dominated by PAH emission and the inner face of the shell defines the destruction radius of PAHs (see §4.1). It is bright because swept-up interstellar dust densities are high here and the dust is exposed to a large flux of soft UV radiation (non-H ionizing photons) that excites PAHs but is not energetic enough to destroy PAHs. The slow fall-off beyond the inner face of the $8\mu\text{m}$ shell represents the PDR region of the bubble, primarily delineated by PAH emission.

Inside the $8\mu\text{m}$ shell, $24\mu\text{m}$, 20 cm, $8.0\mu\text{m}$ and $5.8\mu\text{m}$ emission all peak at the same position, showing that hot dust is present inside the HII region. Note that the $24\mu\text{m}$ emission is saturated at the center. Clearly the stellar wind(s) have not yet succeeded in clearing out or destroying all the dust in the bubble. There is also some diffuse $5.8\mu\text{m}$ and $8\mu\text{m}$ emission inside the bubble. Figure 3 shows that the $3.6\mu\text{m}$ and $4.5\mu\text{m}$ emission vary together because both are dominated by stellar emission. The $5.8\mu\text{m}$ and $8.0\mu\text{m}$ band vary together also, although $5.8\mu\text{m}$ emission is generally fainter than $8.0\mu\text{m}$ emission. The relative distribution of emission at different wavelengths in N10 (i.e. an $8\mu\text{m}$ shell enclosing $24\mu\text{m}$ and radio continuum emission) is a general property of all the bubbles for which we have MAGPIS and MIPS GAL data.

3.2. N21

N21 has a cometary morphology in $8\mu\text{m}$ emission (see Fig 4), but otherwise has similar relative spatial distributions with wavelength as N10 with the exception that N21 is not bounded at $8\mu\text{m}$ along the lower half of the bubble. N21 has a kinematic distance of 3.7 ± 0.6 kpc (Churchwell et al. 2006). At 1.4 GHz it has an integrated flux density of 7.2 Jy and an angular radius of 2.6' (2.8 pc) (Helfand et al. 2006). It requires 8.5×10^{48} ionizing photons s^{-1} to maintain ionization, equivalent to a single O6V star (MSH05).

The $8\ \mu\text{m}$ shell has a radius to the inner face of $2.1'$ ($2.2\ \text{pc}$) and a radius out to the background level of $3.0'$ ($3.2\ \text{pc}$). The clearest perspective on the relative emission distributions with wavelength are the slices at constant longitude (see Fig. 5-6). Figure 5 shows that $8\ \mu\text{m}$ emission is located above the $20\ \text{cm}$ and $24\ \mu\text{m}$ emission. $20\ \text{cm}$ and $24\ \mu\text{m}$ emission increase and decrease in near unison. The $5.8\ \mu\text{m}$ and $8.0\ \mu\text{m}$ emission also vary together (see Figures 5 & 6). $5.8\ \mu\text{m}$ and $8.0\ \mu\text{m}$ are present both inside the bubble and along the top boundary. Inside the bubble, the $8\ \mu\text{m}$ flux is likely dominated by both PAH emission from the front-side and backside of the bubble and by hot dust grains inside the bubble. We measure the integrated flux density at $8\ \mu\text{m}$ inside the $8\ \mu\text{m}$ shell ($0.395^\circ < b < 0.41^\circ$) to be $228\ \text{Jy}$ and the integrated flux density at $24\ \mu\text{m}$ in the same region to be $599\ \text{Jy}$. The former value may be over-estimated by $\sim 30\%$ because of IRAC diffuse calibration errors (Cohen et al. 2007). The dust temperature cannot be determined because of PAH contamination at $8\ \mu\text{m}$.

The relative distributions of hot dust, excited PAHs and the PDR region in N21 is similar to N10. The key difference between N10 and N21 is the absence of $8\ \mu\text{m}$ emission along the southern half of the bubble. The detected $24\ \mu\text{m}$ and $20\ \text{cm}$ emission along the southern interior, however, implies the existence of ionizing photons. The near absence of the $8\ \mu\text{m}$ shell along the lower half of this bubble thus implies the absence of PAHs. This may be because the ambient ISM density in this direction is low enough that the PAHs have either been destroyed by direct exposure to hard stellar UV radiation and/or blown out from the bubble far enough that the PAHs cannot be excited by the stellar radiation due to geometric dilution.

3.3. N49

N49 is a bright MIR bubble surrounding a radio HII region that has an almost spherical structure. It has a kinematic distance of $5.7 \pm 0.6\ \text{kpc}$ (Churchwell et al. 2006). At $1.4\ \text{GHz}$ it has an integrated flux density of $2.8\ \text{Jy}$ and an angular radius out to the background of $1.5'$ ($\sim 2.5\ \text{pc}$) (Helfand et al. 2006). 7.8×10^{48} ionizing photons s^{-1} are necessary to maintain its ionization, equivalent to a single O6V star (MSH05). The radius to the inner face of the $8\ \mu\text{m}$ shell is $1.2'$ ($2.0\ \text{pc}$) and out to the background level is $1.7'$ ($2.3\ \text{pc}$).

N49 has a double-shell structure, the outer traced by $8\ \mu\text{m}$ emission and the inner traced by $24\ \mu\text{m}$ and $20\ \text{cm}$ emission (see Fig 7). As in N10 and N21, $8\ \mu\text{m}$ emission encloses both the $24\ \mu\text{m}$ and $20\ \text{cm}$ emission. The transition between the $8\ \mu\text{m}$ emission ring and the $24\ \mu\text{m}$ and $20\ \text{cm}$ emission ring can be clearly seen in the slice at constant latitude in Fig 8. The $20\ \text{cm}$ and $24\ \mu\text{m}$ emission are coincident, both of which have a central cavity. The $24\ \mu\text{m}/20$

cm dip appears to be the central wind-evacuated cavity expected around early-O stars.

4. Analysis

We propose the following picture for the IR bubbles: ionized gas with a hot dust component is surrounded by a PDR containing swept-up interstellar gas, PAHs, and dust. The ionized gas is traced by 20 cm free-free emission, the hot dust within the HII region is bright at $24\mu\text{m}$ via thermal continuum emission. The IR bubbles are enclosed by a shell of $8\mu\text{m}$ emission dominated by PAH emission features in IRAC bands 3.6, 5.8, and $8.0\mu\text{m}$. The inner face of the $8\mu\text{m}$ shell defines the PAH destruction radius from the central ionizing star(s). In the following sections, we determine the PAH destruction radii and PDR shell thicknesses based on $\frac{5.8\mu\text{m}}{4.5\mu\text{m}}$ and $\frac{8.0\mu\text{m}}{4.5\mu\text{m}}$ flux density ratios.

4.1. PAH Destruction

Povich et al. (2007) argued that ratios of IRAC bands that contain strong PAH emission features ($8.0\mu\text{m}$ and $5.8\mu\text{m}$ bands) to the $4.5\mu\text{m}$ band (which contains no PAH feature) can be used to determine the PAH destruction radius and define the extent of PDRs around hot stars. This technique was applied by Povich et al. (2007) to derive both the PAH destruction region in M17 and the extent of its PDR because the $8.0\mu\text{m}$, $5.8\mu\text{m}$ and $3.6\mu\text{m}$ IRAC bands all contain PAH bands, whereas band-ratios involving the $4.5\mu\text{m}$ PAH-free band should be especially sensitive to regions containing PAHs. They supported their interpretation of these ratios by showing that the $5.8\mu\text{m}/3.6\mu\text{m}$ ratio does not delineate the PDR boundaries. They also presented IRS spectra that proved the disappearance of PAH features within the M17 HII region. Povich et al. (2007) were unable to use the $8.0\mu\text{m}$ images of M17 because the detector was saturated over large regions. We have applied this technique to N10, N21, and N49. The quantitative ratios are different from those toward M17 because M17 is a much more luminous region but the principle is the same. Since N10, N21 and N49 do not saturate the $8.0\mu\text{m}$ detector, we are able to use this band in our analysis as well.

Figs. 9 - 11 show false color images of the $5.8\mu\text{m}/4.5\mu\text{m}$ and $8.0\mu\text{m}/4.5\mu\text{m}$ band ratios, with accompanying longitude or latitude cuts (averaged over 20 pixels) for all three bubbles. We contour the false-color images to indicate the average values that define the PDR regions. For each source, the $5.8\mu\text{m}/4.5\mu\text{m}$ ratio is 6-7 in the bubble interiors, while in the inner edge of the $8\mu\text{m}$ shells (brightest part of the PDR region) it is 9-10. The $8.0\mu\text{m}/4.5\mu\text{m}$ ratio has a slightly larger contrast between the shell and the interior, typically

30-35 versus 23-25, respectively. Using the $5.8 \mu\text{m}/4.5 \mu\text{m}$ ratio to determine the PAH-free region, the bubble interiors have radii of 1.2', 2.2', and 1.5' for N10, N21 and N49, respectively. These are about the same as the radii of the HII regions associated with the bubbles (1.26', 2.6', and 1.5', respectively). The typical radial thickness of the PDR regions are 0.6', 0.6', and 0.3', respectively. Roger & Dewdney (1992) use computer models to show how the ratio of the PDR outer radius to the HII radius is related to the ambient density the bubble is expanding into. Based on the ratios 1.4, 1.1 and 1.2 for N10, N21 and N49, we conclude that ambient density is $\sim 10^3 \text{ cm}^{-3}$. These estimates should be taken with caution, however, since they are not consistent with the estimated T_{eff} of the ionizing star that we determine below (see §5). Lastly, there are also some very conspicuous low ratios (dark spots) in the false color images, especially in the $8\mu\text{m}/4.5\mu\text{m}$ images. These are locations of bright stars, which are bright at $4.5\mu\text{m}$ and much fainter at $5.8\mu\text{m}$ and even fainter at $8.0\mu\text{m}$.

4.2. Dust Temperature

The hot dust in HII regions competes with the gas for stellar UV photons. It also plays an important role in the processing of radiation and cooling of HII regions. It is therefore, of high interest to measure the temperature distribution of the dust as a function of distance from the source(s) of ionization. To do this, it is necessary to estimate what fraction of the $8\mu\text{m}$ emission interior to the inner face of the $8\mu\text{m}$ shell is due to thermal continuum emission as opposed to PAH emission from the front and back sides of the shell. We assume that the PAH emission is confined to a spherical shell of inner radius r and thickness dr , that the PAH emission is proportional to the line-of-sight depth through the shell (front and back) and that emission is homogeneous. With these assumptions, the path length S through the shell at each impact parameter y (which, for objects far from the observer, is directly proportional to the angular separation) is:

$$S = 2 \left(\sqrt{r^2 + 2rdr + dr^2 - y^2} - \sqrt{r^2 - y^2} \right) \quad (1)$$

Figure 12 shows the azimuthally averaged observed radial $8\mu\text{m}$ brightness of N49 with the profile predicted by eq.(1) normalized to the observed flux density at the center of the bubble and superimposed on the observations. Surprisingly, the profile predicted by the assumed simple geometry fits the observations very well. A check on this assumption is the fact that there is no apparent dip in brightness at $8\mu\text{m}$ at the center of N49 but is very apparent at $24\mu\text{m}$ and 20 cm. Taking the good fit of the predicted profile with the

observations at face value implies that almost all the $8\mu\text{m}$ emission interior to the shell is due to PAH emission from the front and back faces of the shell. Only from about $45''$ to $60''$ is there possibly a measurable excess that might be claimed to be thermal continuum emission. If this is the thermal component at $8\mu\text{m}$, it is too small to measure accurately enough to determine the dust temperature. Using the noise level of the $8\mu\text{m}$ emission at the center of the bubble along with the measured $24\mu\text{m}$ emission, we can only place an upper-limit (< 150 K) on the interior dust temperature.

The turndown in $8\mu\text{m}$ brightness beginning at $\sim 80''$ outward indicates the decline in brightness of the PDR. It declines at larger radii because of dilution of stellar photons that can excite the PAH features. We have not done a similar analysis for N21 because of its lack of symmetry.

In N10, on the other hand, there appears to be $8\mu\text{m}$ and $5.8\mu\text{m}$ emission coincident with the central 20 cm peak that is significantly stronger than the shell emission (see Figure 3). This cannot be front or back-face emission, as in N49, but rather it is likely thermal emission from hot dust. Unfortunately, the $24\mu\text{m}$ emission is saturated. Using only the IRAC bands, we can only place an upper-limit (< 250 K) on the interior dust temperature.

4.3. Morphology Comparison

It is instructive to compare the MIR morphology of these three bubbles since they are each unique in interesting ways. The most important difference is that in N10 and N21, $24\mu\text{m}$ and 20 cm emission is centrally peaked, whereas in N49 there is a cavity. That is, the driving star in N49 appears to have evacuated its immediate surroundings of hot dust (as traced by $24\mu\text{m}$ emission) and gas (as traced by 20 cm emission). This difference in hot dust structure could be caused by either N49 containing an earlier ionizing star (O5V vs. O6.5V, see §5) or by a difference in age (N49 being more evolved than N10). A second difference is the detection of $8\mu\text{m}$ emission toward the center of N10 and N21 but its absence toward the center of N49. This difference implies that the dust at the center of N10's and N21 is hotter than in N49.

Since even cooler O stars destroy PAHs in their neighborhood (§4.1), the $8\mu\text{m}$ emission at the centers of N10 and N21 is likely dominated by thermal emission from hot dust. Presumably, small dust grains that give rise to stochastic emission are destroyed near O stars. Assuming that the 24 and $8\mu\text{m}$ emission at the center of N21 are due to thermal emission from large dust grains, we find $T_{dust} \sim 200$ K. A similar estimate cannot be made for N10 because the $24\mu\text{m}$ emission is saturated; however, using 5.8 and $3.5\mu\text{m}$ emission,

which probably samples hotter dust still closer to the central star than in N21, we find $T_{dust} \sim 380$ K for N10. The dust temperatures in N21 and N10 are higher than in N49 even though N49 is ionized by a hotter star because the dust is much closer to the central star(s) in N10 and N21 than in N49.

5. Associated YSOs and Ionizing Stars

In this section, we examine the stellar populations observed at NIR-MIR wavelengths toward each bubble. We are interested in the YSOs associated with each bubble, especially those appearing on the bubble rims that may have been triggered by the expanding bubble, as well as the ionizing stars responsible for producing each bubble.

To identify YSO candidates, we fit GLIMPSE Archive sources combined with $24 \mu\text{m}$ photometry from MIPS GAL images with spectral energy distributions (SEDs) from a large, pre-computed grid of YSO models (Robitaille et al. 2006). The grid consists of 20,000 2-D Monte Carlo radiation transfer models (Whitney et al. 2003a,b; Whitney et al. 2004) spanning a complete range of stellar mass and evolutionary stage and output at 10 viewing angles (a total of 200,000 SEDs). The model fitting tool uses a fast χ^2 -minimization fitting algorithm (Robitaille et al. 2007) and includes a grid of Kurucz (1993) stellar photosphere SEDs. We can robustly distinguish between YSOs and extincted photospheres of main-sequence and giant stars because YSOs require a thermal emission component from circumstellar dust to reproduce the shapes of their mid-IR excesses. The concept of fitting SEDs from a large grid of models was tested by fitting the SEDs of several known YSOs in Taurus and deriving physical properties in agreement with previous determinations based on other methods (Robitaille et al. 2007). This model-based approach does a reliable job of identifying YSO candidates, and additionally provides information on the physical properties of the YSOs.

In Table 1 we present the YSO candidates listed in order of ascending Galactic longitude for each bubble. For each YSO candidate, the set of well-fit models (numbering N_{fits}) was selected on the basis of χ^2 according to

$$\chi^2 - \chi_{\text{min}}^2 \leq 2N_{\text{data}}, \quad (2)$$

where χ_{min}^2 is the goodness-of-fit parameter of the best-fit model and $4 \leq N_{\text{data}} \leq 8$ is the number of flux datapoints used for the fit. From the set of well-fit models we construct the cumulative probability distributions of the YSO parameters. These include mass M_{\star} of the central star, total luminosity (stellar plus disk accretion) L_{TOT} of the YSO, and envelope accretion rate \dot{M}_{env} . In Table 1 we report the “best” values of these YSO parameters, defined as the value of each parameter for which the slope of the cumulative probability distribution

is maximized. We include the minimum and maximum parameter values representing 95% confidence intervals. Table 1 includes the most probable evolutionary stage of the YSO, a classification of the models introduced by Robitaille et al. (2006) that parallels the observational “Class” taxonomy (Lada 1987). A Stage I YSO is heavily embedded in its infalling envelope, while a Stage II YSO is a more evolved disk-dominated object. We do not detect any candidate Stage III objects, young stars with remnant dust disks. This may be a selection effect, however, because the SEDs of such sources tend to most closely resemble stellar photospheres, and we have been conservative in our selection of YSO candidates. The comments column of Table 1 gives the apparent location of the YSO: (Rim) YSO on the projected rim of the bubble and hence a possible example of triggered star formation; (IRDC) YSO within an infrared dark cloud; (Bub) YSO inside the bubble in projection; and (PDR) YSO within the bright diffuse PAH emission from the PDR of the bubble. We also include a [4.5] flag for two YSO candidates that appear to be associated with bright, extended emission at 4.5 μm . Excess emission in IRAC [4.5] probably indicates shocked molecular (H_2 or CO) outflow or jet, a signpost of the early stages of massive star formation (Smith et al. 2006; Davis et al. 2007; Shepherd et al. 2007).

Identifying each bubble’s ionizing stars is complicated by the fact that such stars, while characteristically luminous, have reddened Rayleigh-Jeans spectral slopes at NIR–MIR wavelengths. While the stellar photosphere models included in the fitting tool are primarily intended to facilitate the separation of YSO candidates from field stars, it is possible to use the results of the photosphere fits to identify candidate ionizing stars lying within the bubbles. Robitaille et al. (2007) have incorporated into the fitting tool an interstellar extinction model using the MIR extinction properties derived by Indebetouw et al. (2005). To identify candidate hot stars in the bubble, we forced the minimum extinction used by the fitting tool to be 8–10 mag and selected sources for which the best-fit Kurucz model had a photospheric temperature $T_{\text{eff}} > 20,000$ K. This revealed ~ 10 candidate ionizing stars within the boundaries of each bubble. We then fit these sources a second time, allowing the extinction to range from 0–30 mag. The resulting set of well-fit models, selected according to Equation 2, produces a tight curve of T_{eff} versus stellar radius R when scaled to the distance of the bubble. This curve intersects with the theoretical O-star $T_{\text{eff}}-R$ relations of MSH05 (see Fig. 13). This selects a particular group of models, providing estimates of both the spectral types and the extinction toward each of the candidate ionizing stars in each bubble. The results of this analysis are presented in Table 2. The candidate stars are listed in decreasing order of their likely importance in ionizing the H II regions of the bubbles. The fifth column indicates our best estimate of the ionizing star based on location, spectral type and radio continuum emission. It is important to note that this method of assigning spectral type is not definitive. Any one of the candidate ionizing stars could be a less reddened, foreground,

cooler main sequence star or red giant. Geometrical arguments, however, strongly support the identification of the best candidates as real O stars responsible for producing the bubbles.

5.1. N10

Out of 687 GLIMPSE Archive sources analyzed within a 3.6' (5.2 pc) radius from the center of N10, 15 were fit with high confidence by YSO models. These YSO candidates surround N10 (yellow circles in Figure 14), and the configuration is highly suggestive of triggered massive star formation. The bubble is bordered on 2 sides by infrared dark clouds (IRDCs). 4 candidate highly-embedded Stage I massive YSOs appear to be located on the bubble rims (sources N10-7, 5.8–16.7 M_{\odot} ; N10-9, 8.3–13.5 M_{\odot} ; N10-11, 8.4–12.7 M_{\odot} ; and N10-12, 8.9–17.1 M_{\odot} , see Table 1). Two of these YSOs are also in an IRDC and the other two YSOs appear close to an IRDC.

Four stars have been identified as possible ionizing stars located in projection inside the bubble. It should be emphasized that these stars are well-fit with stellar photospheres and are not YSOs. The spectral energy distributions of these stars suggest spectral types ranging from O7.5V to O6V (see Table 2 and cyan circles in Figure 19). Although the spectral types are rather uncertain, if we take them at face value and use the models of MSH05, their combined UV photon flux is $\sim 2.2 \times 10^{49} \text{ s}^{-1}$, more than adequate to maintain ionization of the HII region ($1.6 \times 10^{49} \text{ s}^{-1}$, based on 20 cm emission). Some UV, however, is required to heat the dust at the center of N10. IN10-1 appears to lie at the center of the bubble and near the center of the radio and saturated diffuse 24 μm emission filling the bubble, while IN10-2 appears to lie in a sub-cavity near a second peak of bright diffuse MIR emission that may be hiding a cluster of later-type OB stars or YSOs. Preliminary optical spectroscopy obtained using the Wyoming Infrared Observatory (WIRO) indicates that IN10-3 is an O8-B0 V star (Kobulnicky, priv. comm.). Thus, the above method appears to be a robust method of identifying ionizing star candidates. The discrepancy between the spectral identification and the analysis presented above may be caused by the uncertain kinematic distance used for the bubble. The presence of the IRDCs on 2 sides of N10 suggest that this bubble may be density-bounded in those directions, allowing the bubble to expand asymmetrically, with the center of influence from these 2 stars offset from the geometric center of the bubble.

5.2. N21

N21 is associated with a larger HII region complex. While 21 YSO candidates (yellow circles in Figure 15) were selected from the 2333 GLIMPSE Archive sources within 6' (6.5 pc, white circle) from the center of the bubble, more YSO candidates probably lie beyond our search radius. The greatest concentration of YSOs appears in the IRDC located midway between N21 and a neighboring bubble in the upper-left corner of Figure 15 (N22 in the Churchwell et al. 2006 catalog), but it is unclear whether this IRDC is physically associated with either of the bubbles. Perhaps the most interesting single point source in this image is the very bright greenish-red source that appears to lie inside the bubble. This source has an extremely positive spectral index in the NIR–MIR (it is undetected in 2MASS J and H and saturated in all 4 GLIMPSE bands) and is bright enough at longer MIR wavelengths to be detected in all 4 MSX bands and to saturate the MIPS 24 μm band. Although this spectral index is suggestive of a massive Class I YSO, this source is undetected by MIPS at 70 μm , while a YSO SED should peak near 70 μm . We can estimate ranges of extinction and distance consistent with the source being an AGB star by assuming a typical K-magnitude of -7.56 (Sohn et al. 2006). Assuming $A_V < 40$ mag (larger than any source detected in the field), the distance is > 10 kpc, indicating a background AGB star.

The best candidate star for producing N21 is IN21-1, which lies at the center of the brightest radio and diffuse 24 μm emission. The model fits to this star, when scaled to the 3.7 kpc kinematic distance of the H II region, produce a stellar radius too large to be a main-sequence star (see Fig 13). Instead, the models lie exactly along the $T_{\text{eff}}-R$ curve derived by MSH05 for O supergiants, a highly suggestive correspondence. Because the 2 curves overlap the spectral type is degenerate. Preliminary optical spectroscopy obtained using WIRO indicates IN21-1 is a late-O supergiant (Kobulnicky, priv. comm.), again confirming the method of identifying ionizing star candidates. The ionizing photon flux required to maintain the H II region suggests an early BI.

5.3. N49

Within a radius of 3.6' (6 pc) from the center of N49, 722 GLIMPSE Archive sources were analyzed and 7 were fit with high confidence as YSOs (yellow circles in Figure 16). N49-1 (see Table 1 and Figure 17) was fit with Stage I models ranging in mass from 14 to 29 M_{\odot} , making it potentially the most massive YSO in our sample. N49-3 sports a spectacular example of a bipolar outflow seen in 4.5 μm emission. Both YSO candidates appear to lie in an IRDC just beyond the rim of the bubble and adjacent to a bright knot of diffuse 8.0 μm and 24 μm emission that probably hides additional YSOs undetected by GLIMPSE because

they are masked by the diffuse MIR emission. Other potential YSOs in the IRDC may not have been detected by GLIMPSE due to confusion and high extinction. Hence N49-1 and N49-3 may be massive members of a YSO cluster that has been triggered by the expansion of the bubble.

N49 contains a star, IN49-1, at the center of the wind-evacuated cavity (Figure 16). Given the strong circular symmetry observed in all bands, this star is very likely the ionizing star responsible for producing the bubble. IN49-1 is fit both by an O8 III and an O5 V star (see Fig 13). The UV photon flux implied by the radio emission ($10^{48.89} \text{ s}^{-1}$) is in closer agreement with an O8 III star ($10^{48.88} \text{ s}^{-1}$) than an O5 V star ($10^{49.22} \text{ s}^{-1}$). However, the age implied by the presence of triggered star-formation is closer to that of an O5 V star ($\sim 10^5$ yrs) than that of an O8 III star (10^6 yrs), so we favor the O5 V classification. Presumably the excess UV is responsible for heating the dust that produces the $24 \mu\text{m}$ emission inside the HII region. The model SEDs fit to the 2 brightest sources (N49-1 and N49-3) were based upon the 4 IRAC bands plus a $24 \mu\text{m}$ lower limit. The $24 \mu\text{m}$ lower limit effectively places lower limits on the YSO masses and luminosities, but the upper limits are difficult to constrain based upon the available photometry.

The central cavity in N49 seems to indicate that this bubble is stellar wind-dominated and therefore should be describable by the analytic relations of Weaver et al. (1977):

$$R(t) \propto n_o^{-\frac{1}{5}} L_w^{\frac{1}{5}} t^{\frac{3}{5}}$$

where $R(t)$ is the radius, n_o is the initial ambient density, L_w is the stellar wind luminosity, and t is the dynamical age of the bubble. From this, one can estimate the age of a bubble as a function of n_o given the wind luminosity and a measured radius. We use the stellar parameters of MSH05 to estimate the mass loss rate ($1.5 \times 10^{-6} M_\odot \text{ yr}^{-1}$) and wind luminosity of the ionizing star ($\sim 4 \times 10^{36} \text{ erg s}^{-1}$) using the prescription of Vink, de Koter, and Lamers (2001). Having the wind luminosity and measured bubble radius, we can estimate the age of the bubble for an assumed ambient density. Several Class I or younger YSOs have been identified along the periphery of the bubble. Assuming that the YSOs were triggered by the expansion of the bubble would require the bubble to be at least 10^5 yr old because this is the time scale for massive YSO formation. Using the estimated initial ambient density of $\geq 10^3 \text{ cm}^{-3}$, the Weaver et al. (1977) relations implies a dynamical age $\geq 10^5$ yr, a very young bubble but easily old enough to have spawned a second generation of star formation. Freyer et al. (2006), however, have shown using numerical simulations that the energy transfer efficiency may be lower than assumed in analytic models. If this is the case, then the age estimates based on the analytic relations will be under-estimated, giving even more time for triggered star formation to occur.

6. Conclusions

Based on MIR and 20 cm observations of three bubbles, we conclude the following:

- At the center of each bubble there is a region containing ionized gas and hot dust delineated by radio free-free emission and 24 μm emission, respectively.
- At the center of N10 and N21 (but not N49), the hot dust is also traced by 5.8 and 8.0 μm emission.
- Based on the decreased ratio of 8.0 μm /4.5 μm , 5.8 μm /4.5 μm and the lack of a similar decrease in 8.0 μm /3.6 μm , we conclude that inside the 8 μm shell PAHs are destroyed by hard, direct stellar UV radiation.
- Based on the increased 8.0 μm /4.5 μm , 5.8 μm /4.5 μm , the bright 8.0 μm ring emission is dominated by PAH emission that defines the PDR region around each bubble.
- We have identified YSO candidates and probable ionizing sources for each bubble. This was accomplished by employing the SED model fitter developed by Robitaille et al. (2007) to fit model SEDs of YSOs and hot stellar photospheres (Kurucz 1993) to the observed fluxes.
- Based on morphology and environment, several of the identified YSO candidates in N10 and N49 appear to be triggered by expansion of the bubbles.
- The wind-blown cavity at the center of N49 appears to be produced by a central O5 V star, the hottest ionizing star observed here. This bubble appears to be dominated by the wind from the O5 star and have a dynamical age of $\geq 10^5$ yrs.

We would like to acknowledge Chip Kolbunicky for obtaining optical spectra of the candidate ionizing stars. An anonymous referee made many comments which improved the paper. E.B.C would like to acknowledge support through NASA contract # 1275394.

REFERENCES

- Benjamin, R. A., et al. 2003, *PASP*, 115, 953
- Carey, S. J., et al. 2005, *Bulletin of the American Astronomical Society*, 37, 1252
- Castor, J., McCray, R., & Weaver, R. 1975, *ApJ*, 200, L107
- Capriotti, E.R. & Kozminski, J.F. 2001, *PASP*, 113, 677
- Churchwell, E., & GLIMPSE Team 2001, *Bulletin of the American Astronomical Society*, 33, 821

- Churchwell, E., et al. 2006, ApJ, 649, 759
- Churchwell, E., et al. 2007, ApJ, submitted
- Cohen, M., et al. 2007, MNRAS, 374, 979
- Davis, C. J., Kumar, M. S. N., Sandell, G., Froebrich, D., Smith, M. D., & Currie, M. J. 2007, MNRAS, 374, 29
- Deharveng, L., Zavagno, A., & Caplan, J. 2005, A&A, 433, 565
- Draine, B. T. 2003, ARA&A, 41, 241
- Fazio, G.G., et al. 2004 ApJS, 154, 87
- Freyer, T., Hensler, G., & Yorke, H. W. 2003, ApJ, 594, 888
- Freyer, T., Hensler, G., Yorke, H.W. 2006, ApJ, 628, 262 [FHY06]
- Garcia-Segura, G., & Franco, J. 1996, ApJ, 469, 171
- Hoare, M. G. 1990, MNRAS, 244, 193
- Hoare, M. G., Roche, P. F., & Glencross, W. M. 1991, MNRAS, 251, 584
- Hoare, M. G., Kurtz, S. E., Lizano, S., Keto, E., & Hofner, P. 2007, Protostars and Planets V, 181
- Helfand, D. J., Becker, R. H., White, R. L., Fallon, A., & Tuttle, S. 2006, AJ, 131, 2525
- Indebetouw, R. et al. 2005, ApJ, 619, 931
- Kassis, M., Adams, J. D., Campbell, M. F., Deutsch, L. K., Hora, J. L., Jackson, J. M., & Tollestrup, E. V. 2006, ApJ, 637, 823
- Kessler, M. F., et al. 1996, A&A, 315, L27
- Kröger, D., Hensler, G., Freyer, T., 2006 A&A, 450, L5
- Kröger, D., Freyer, T., Hensler, G., Yorke, H.W. 2007 A&A, submitted
- Kurucz, R. L. 1993, VizieR Online Data Catalog, 6039, 0
- Lada, C. J. 1987, in IAU Symp. 115: Star Forming Regions, eds. M. Peimbert & J. Jugaku,

- Martins, F., Schaerer, D., Hillier, D.J. 2005, *A&A*, 436, 1049
- Peeters, E., Tielens, A. G. G. M., Allamandola, L. J., Bauschlicher, C. W., Boogert, A. C. A., Hayward, T. L., Hudgins, D. M., & Sandford, S. A. 2003, *Astrophysics of Dust* p.42
- Peeters, E., Martín-Hernández, N. L., Rodríguez-Fernández, N. J., & Tielens, X. 2005, *Space Science Reviews*, 119, 273
- Povich, M. S., et al. 2007, *ApJ*, 660, 346
- Price, S.D., Egan, M.P., Carey, S.J., Mizuno, D., Kuchar, T. 2001, *A&A*, 121, 2819
- Rieke, G. H., et al. 2004, *ApJS*, 154, 25
- Robitaille, T. P., Whitney, B. A., Indebetouw, R., Wood, K., & Denzmore, P. 2006, *ApJS*, 167, 256
- Robitaille, T. P., Whitney, B. A., Indebetouw, R., & Wood, K. 2007, *ApJS*, 169, 328
- Smith, H. A., Hora, J. L., Marengo, M., & Pipher, J. L. 2006 *ApJ*, 645, 1264
- Shepherd, D. S. et al. 2007, *ApJ*, submitted
- Sohn, Y.-J., Kang, A., Rhee, J., Shin, M., Chun, M.-S., & Kim, H.-I. 2006, *A&A*, 445, 69
- Weaver, R., McCray, R., Castor, J., Shapiro, P., Moore, R. 1977, *ApJ*, 218, 377
- Werner, M. W., et al. 2004, *ApJS*, 154, 1
- Whitney, B. A., Wood, K., Bjorkman, J. E., & Wolff, M. J. 2003, *ApJ*, 591, 1049
- Whitney, B. A., Wood, K., Bjorkman, J. E., & Cohen, M. 2003, *ApJ*, 598, 1079
- Whitney, B. A., Indebetouw, R., Bjorkman, J. E., & Wood, K. 2004, *ApJ*, 617, 1177
- Whitworth, A.P., Bhattal, A.S., Chapman, S.J., Disney, J.J. & Turner, J.A. 1994, *MNRAS*, 268, 291
- Vink, J.S., deKoter, A., Lamers, H.J.G.L. 2001, *A&A*, 369, 574

Fig. 1.— N10, 24 μm (red), 8 μm (green) and 4.5 μm (blue). 20 cm (contours) in bottom panel. Note that the 24 μm emission is saturated at the center of the image. The white dashed line on the top figure indicates the location of the cross-cut in figures 2-4.

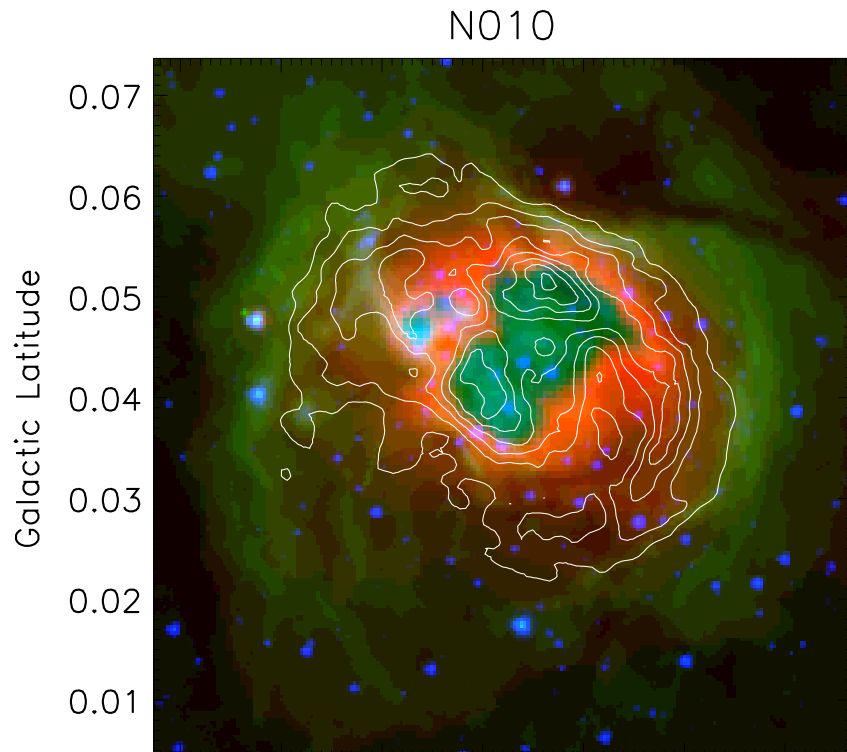
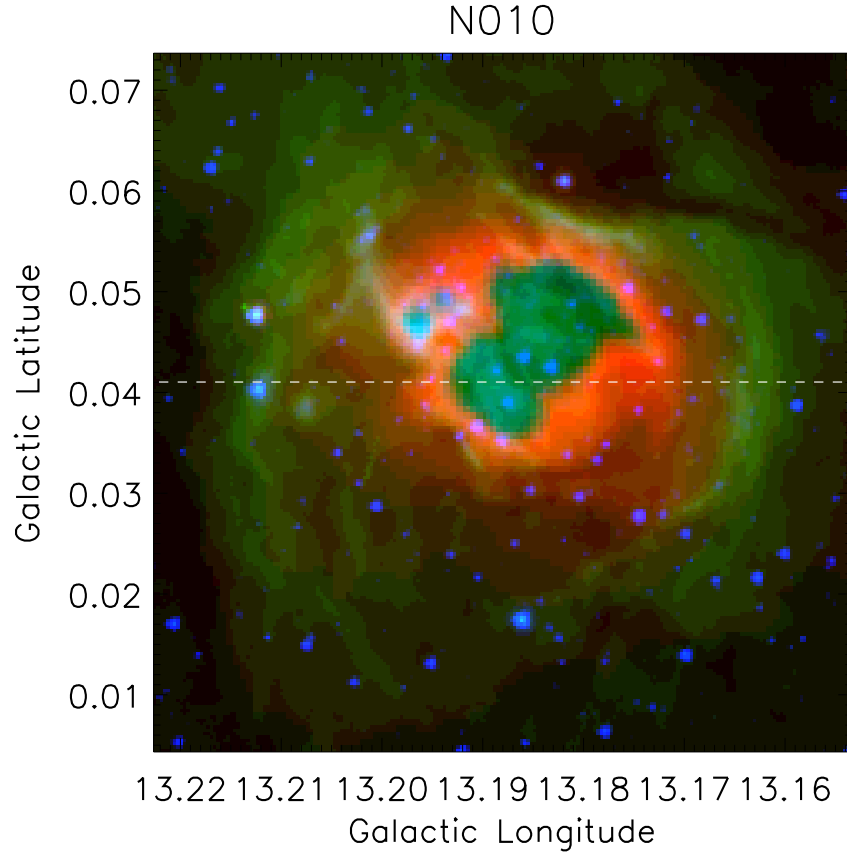


Fig. 2.— N10: Slice at latitude $b=0.04^\circ$. 20 cm (solid, magnified 10^6), 24 μm (dotted) and 8 μm (dashed, magnified 5x). The location of the 8 μm shell and central 24 μm hot dust emission are indicated. Note that the 24 μm emission is saturated in the center of the slice, resulting in the strong dip and missing data between longitudes 13.18° and 13.20° .

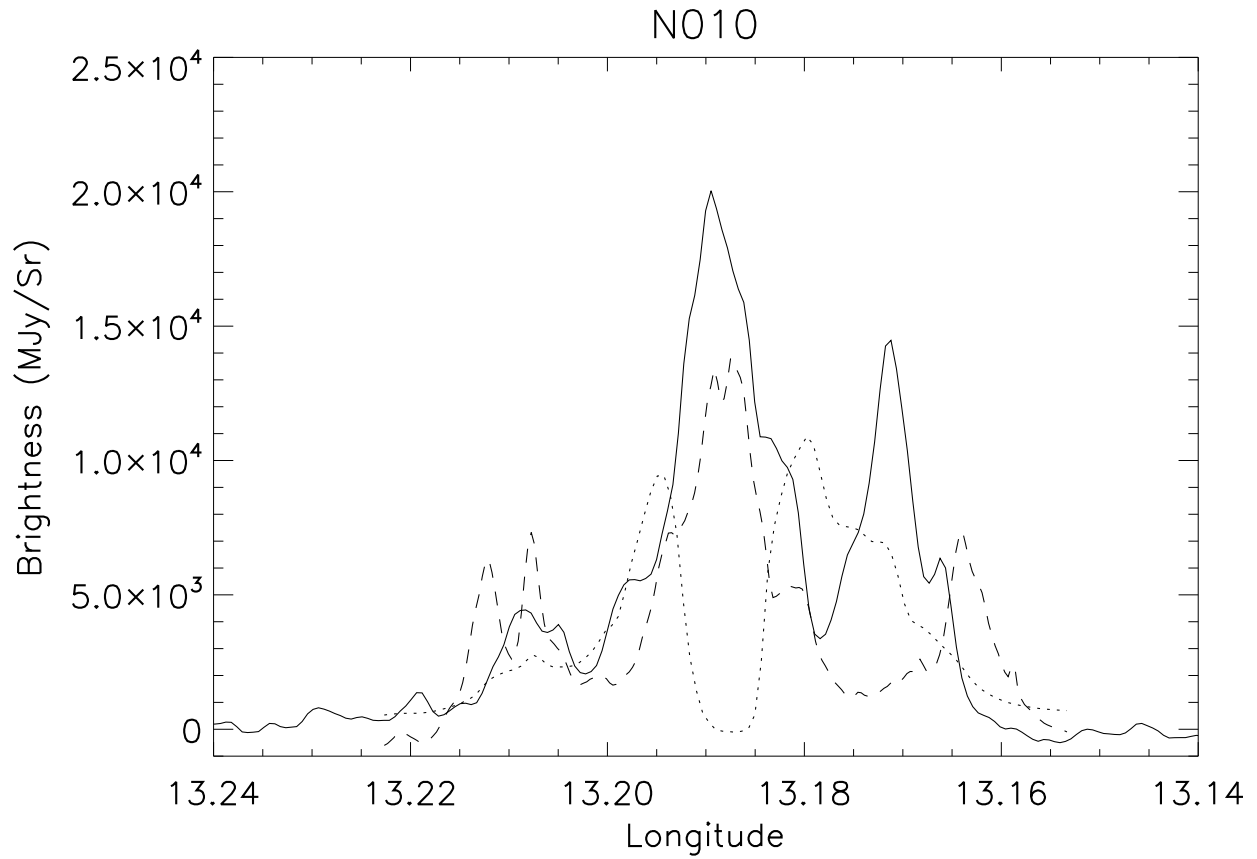


Fig. 3.— N10: Slice at latitude $b=0.04^\circ$. $3.6 \mu\text{m}$ (solid), $4.5 \mu\text{m}$ (dotted) and $5.8 \mu\text{m}$ (dashed). The spikes in $3.6 \mu\text{m}$ and $4.5 \mu\text{m}$ emission indicate stars.

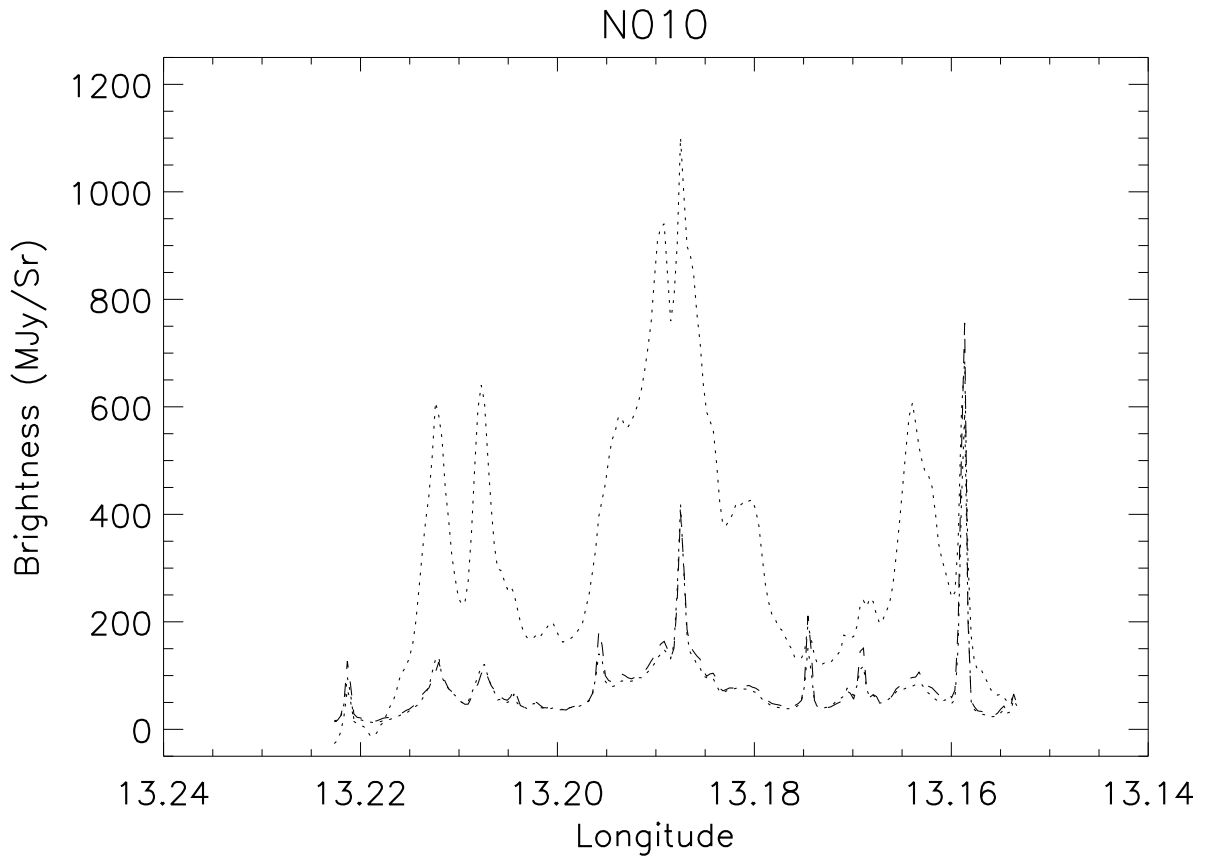


Fig. 4.— N21, 24 μm (red), 8 μm (green), 4.5 μm (blue) and 20 cm (contours) in the bottom panel. The white dashed line on the top figure indicates the location of the cross-cut in figures 6 & 7.

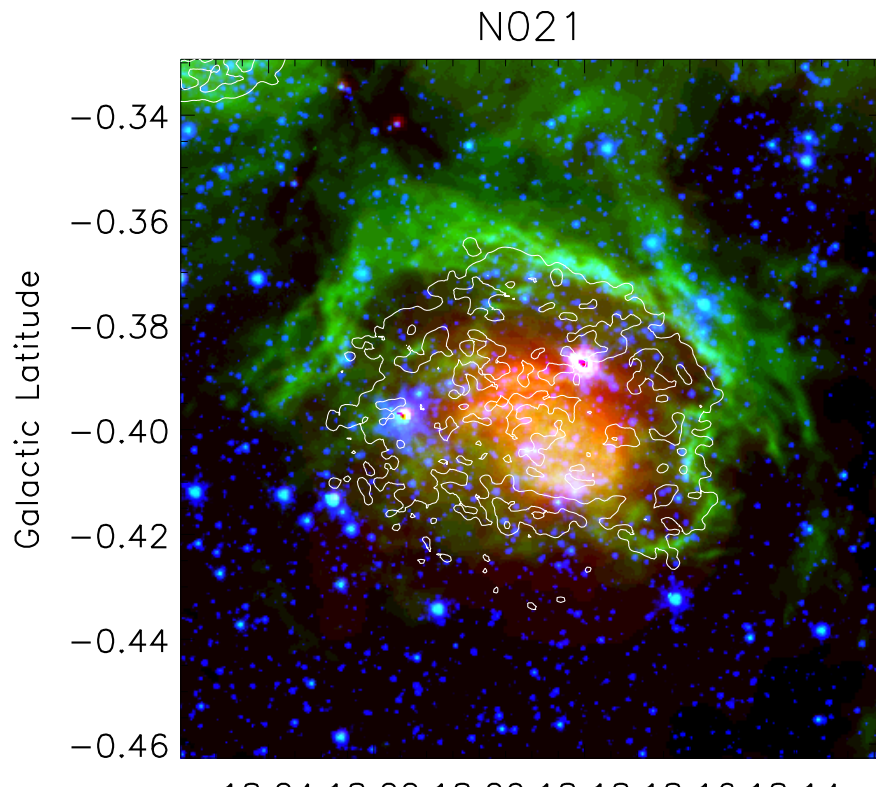
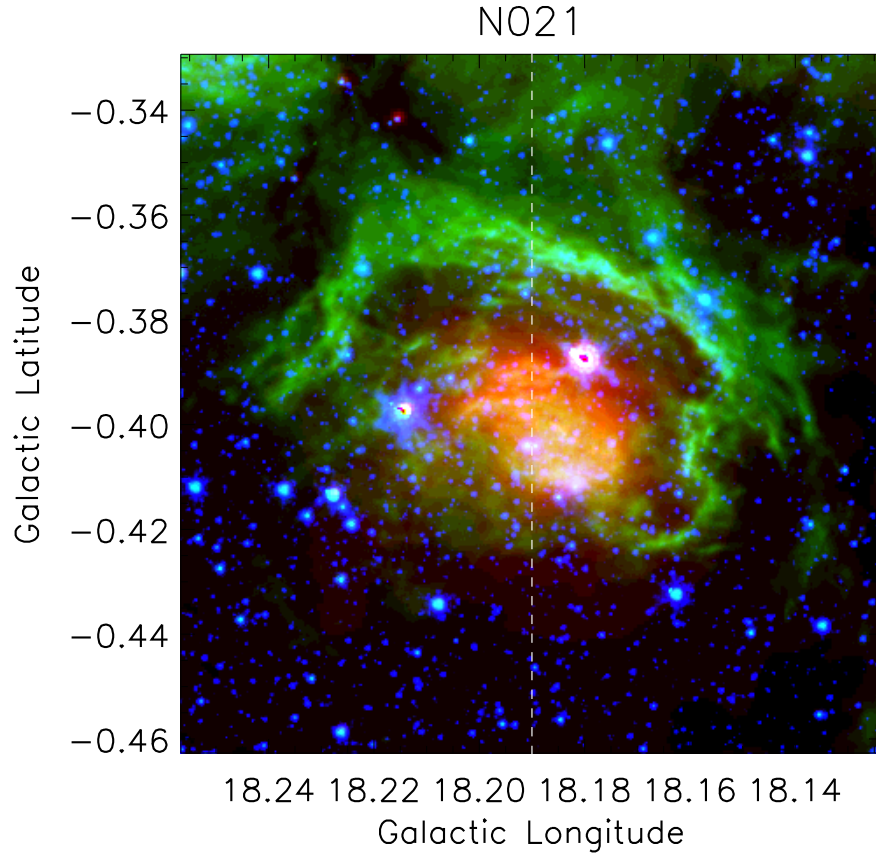


Fig. 5.— N21: Slice at longitude $l=18.19^\circ$. 20 cm (solid, magnified 10^6x), $24 \mu\text{m}$ (dotted) and $8 \mu\text{m}$ (dashed, magnified $5x$)

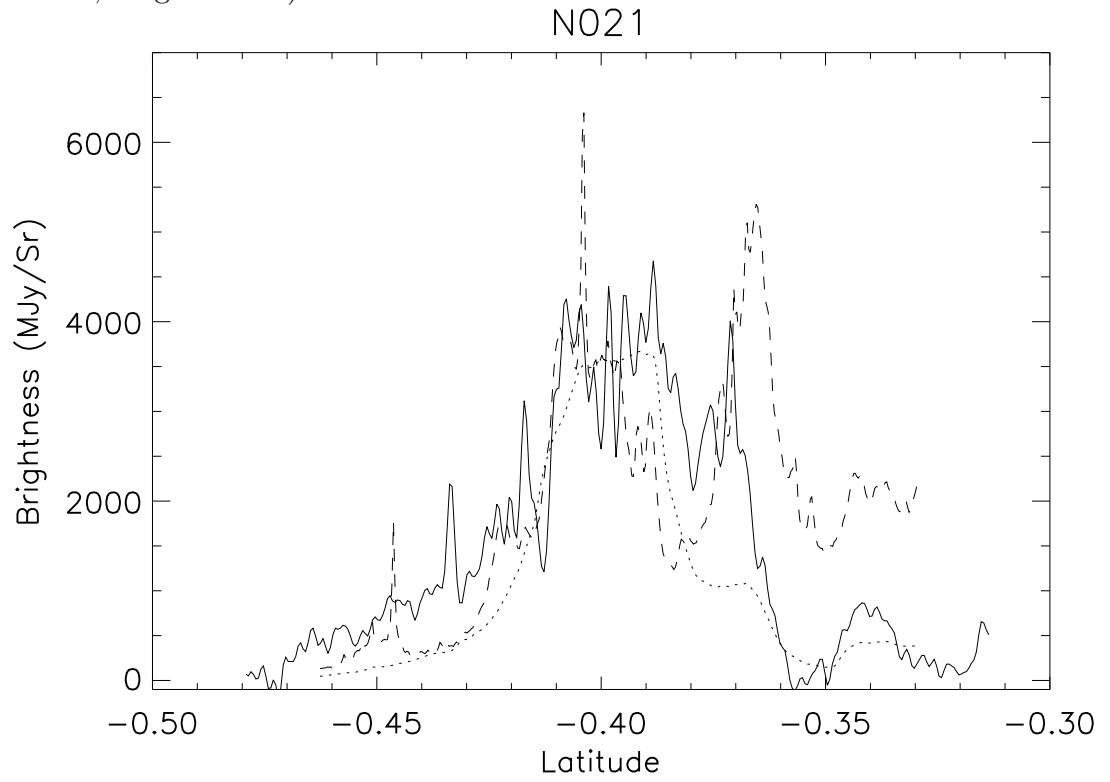


Fig. 6.— N21: Slice at longitude $l=18.19^\circ$. $3.6 \mu\text{m}$ (solid), $4.5 \mu\text{m}$ (dotted) and $5.8 \mu\text{m}$ (dashed). The spikes in $3.6 \mu\text{m}$ and $4.5 \mu\text{m}$ emission indicate stars.

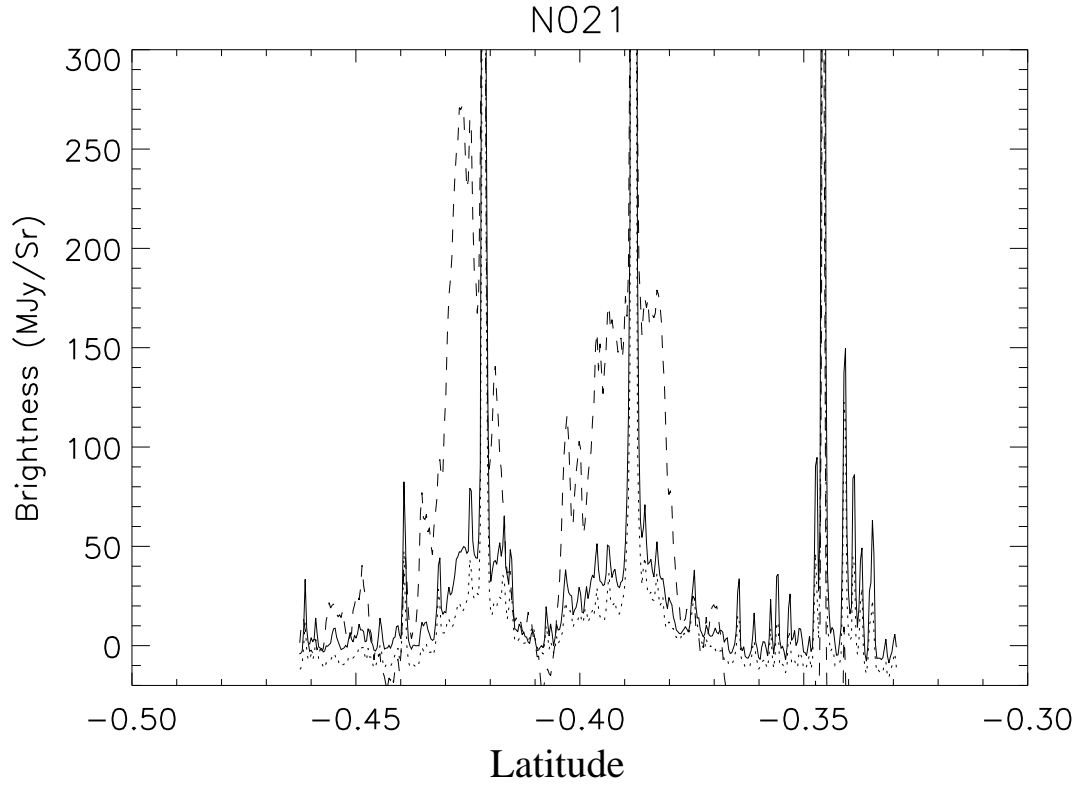


Fig. 7.— N49, 24 μm (red), 8 μm (green), 4.5 μm (blue) and 20 cm (contours) in bottom panel. The white dashed line on the top figure indicates the location of the cross-cut in figures 10 & 11.

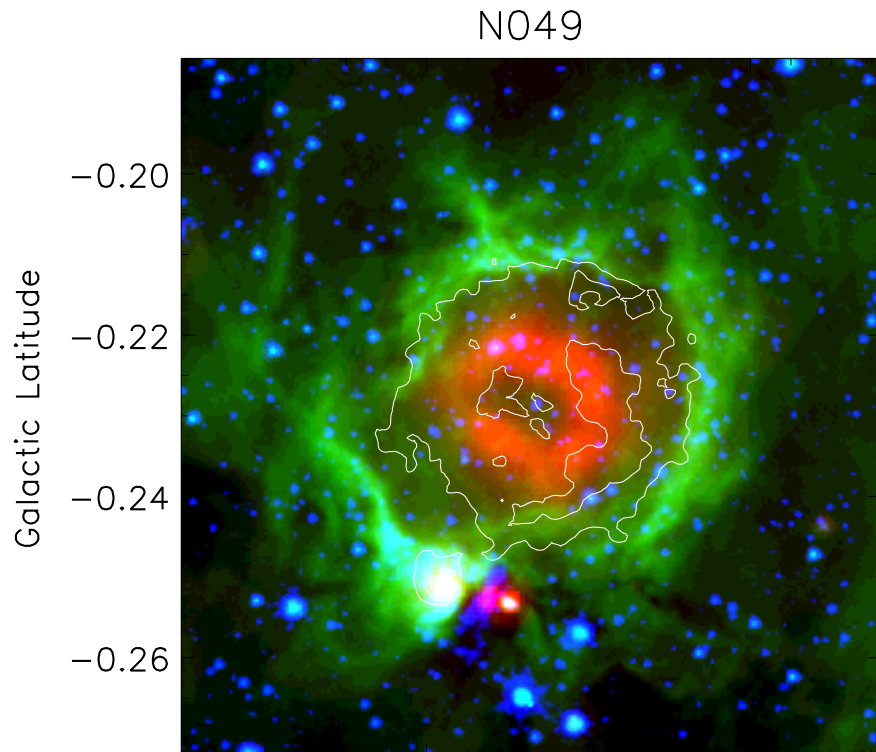
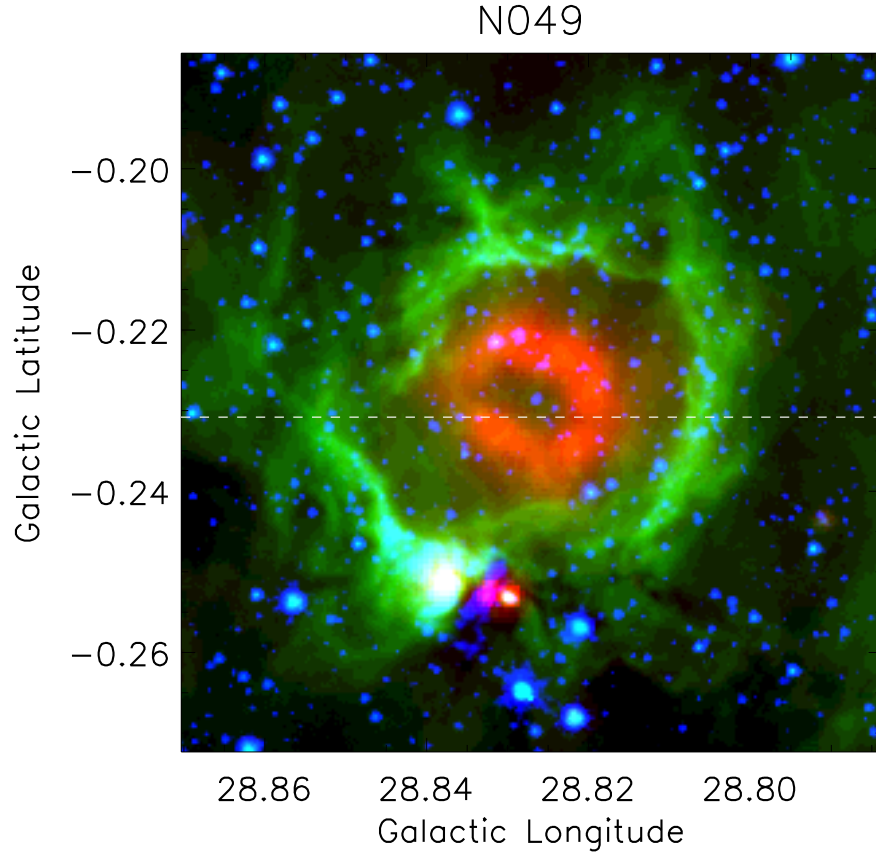


Fig. 8.— N49: Slice at latitude $b=-0.23^\circ$. 20 cm (solid, magnified 10^6x), $24 \mu\text{m}$ (dotted) and $8 \mu\text{m}$ (dashed, magnified 5x). Note that there is no central peak at $24 \mu\text{m}$ as there is in N10 and N21.

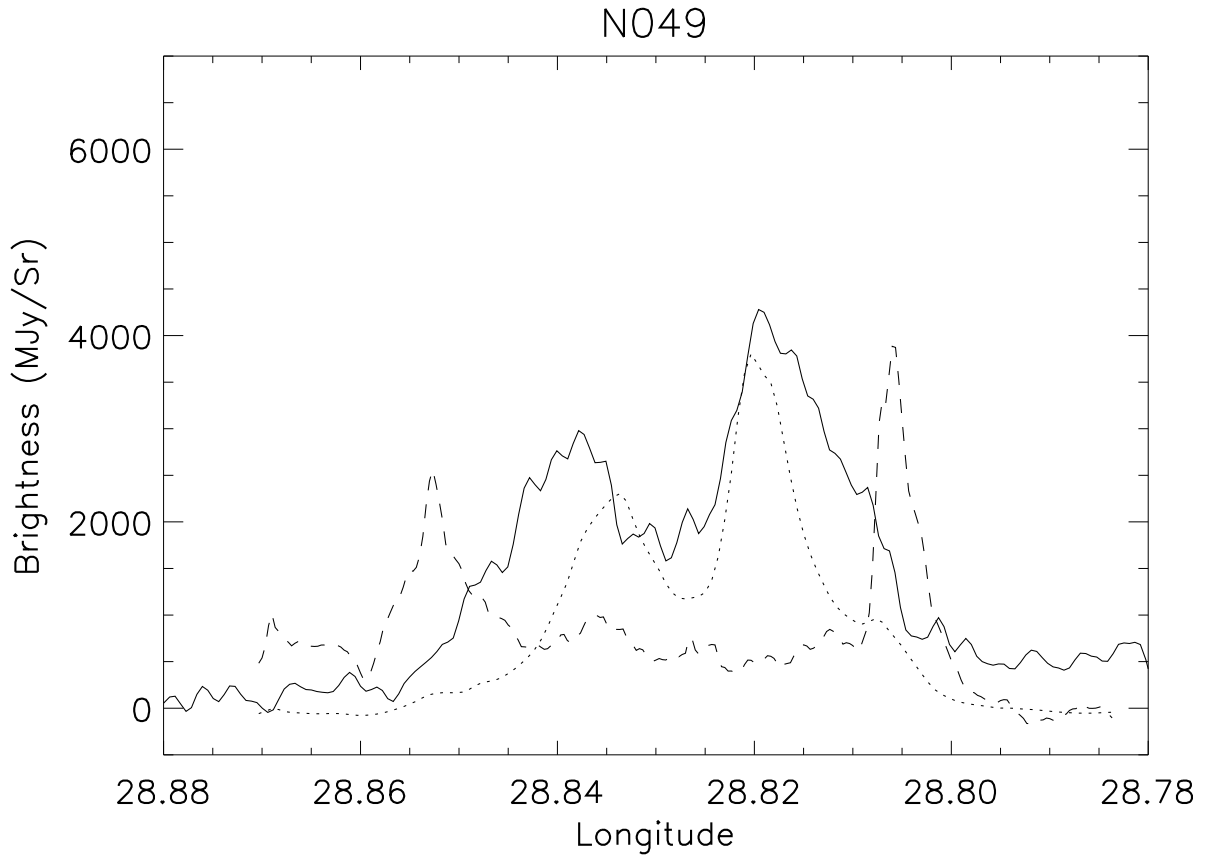


Fig. 9.— N10: PAH destruction as measured from $5.8 \mu\text{m} / 4.5 \mu\text{m}$ (upper-left) and $8.0 \mu\text{m} / 4.5 \mu\text{m}$ (lower-left). The color scale ranges from 5 to 12 (upper-left, blue-to-red) and 24 to 44 (lower-left, blue-to-red). The contours represent ratios of 8.5 (upper-left) and 25 (lower-left). Dashed white lines at left indicate position of slices show at right.

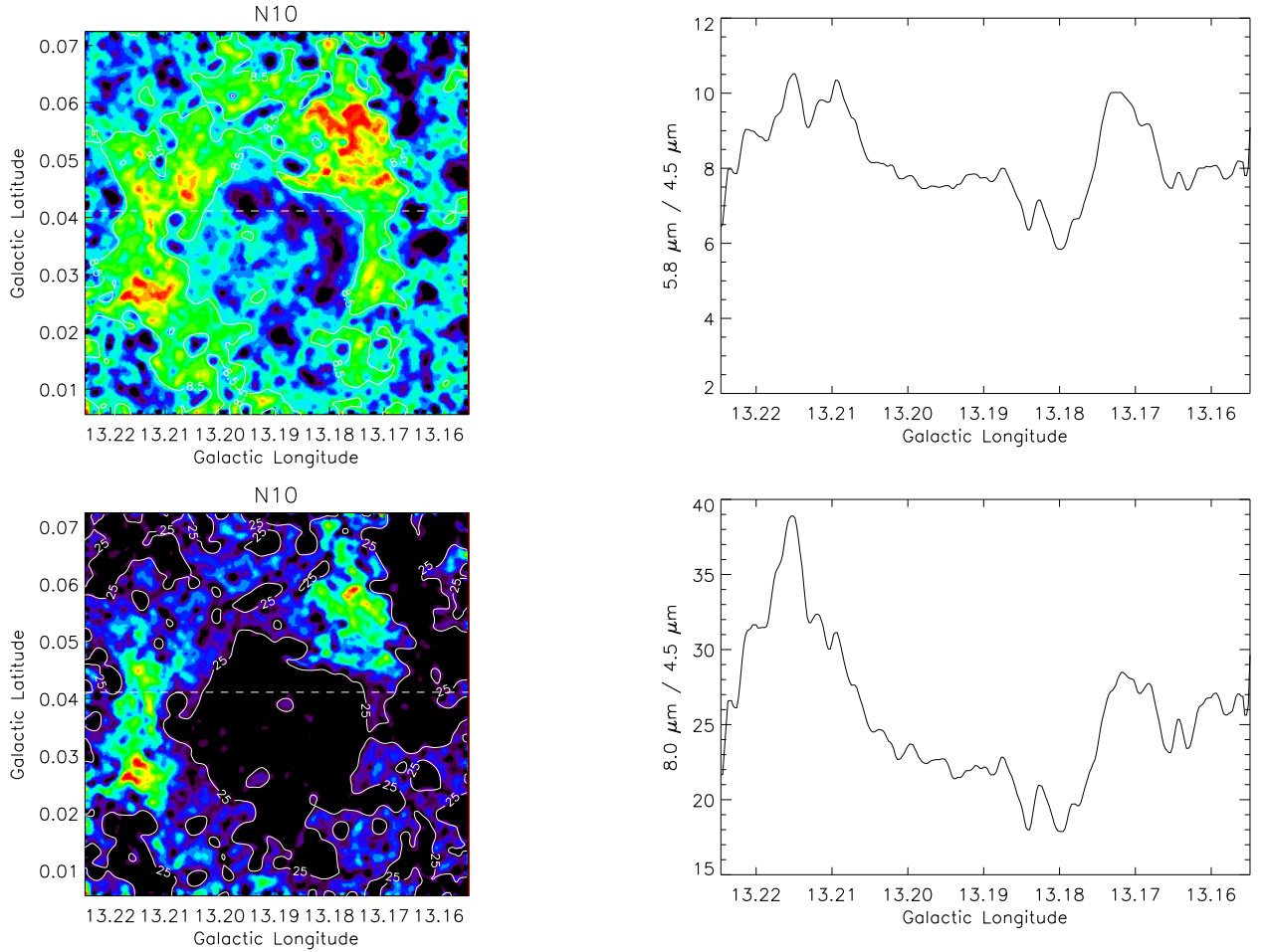


Fig. 10.— N21: PAH destruction as measured from $5.8 \mu\text{m} / 4.5 \mu\text{m}$ (upper-left) and $8.0 \mu\text{m} / 4.5 \mu\text{m}$ (lower-left). The color scale ranges from 4 to 12 (upper-left, blue-to-red) and 15 to 40 (lower-left, blue-to-red). The contours represent ratios of 7.5 (upper-left) and 25 (lower-left). Dashed white lines at left indicate position of slices show at right.

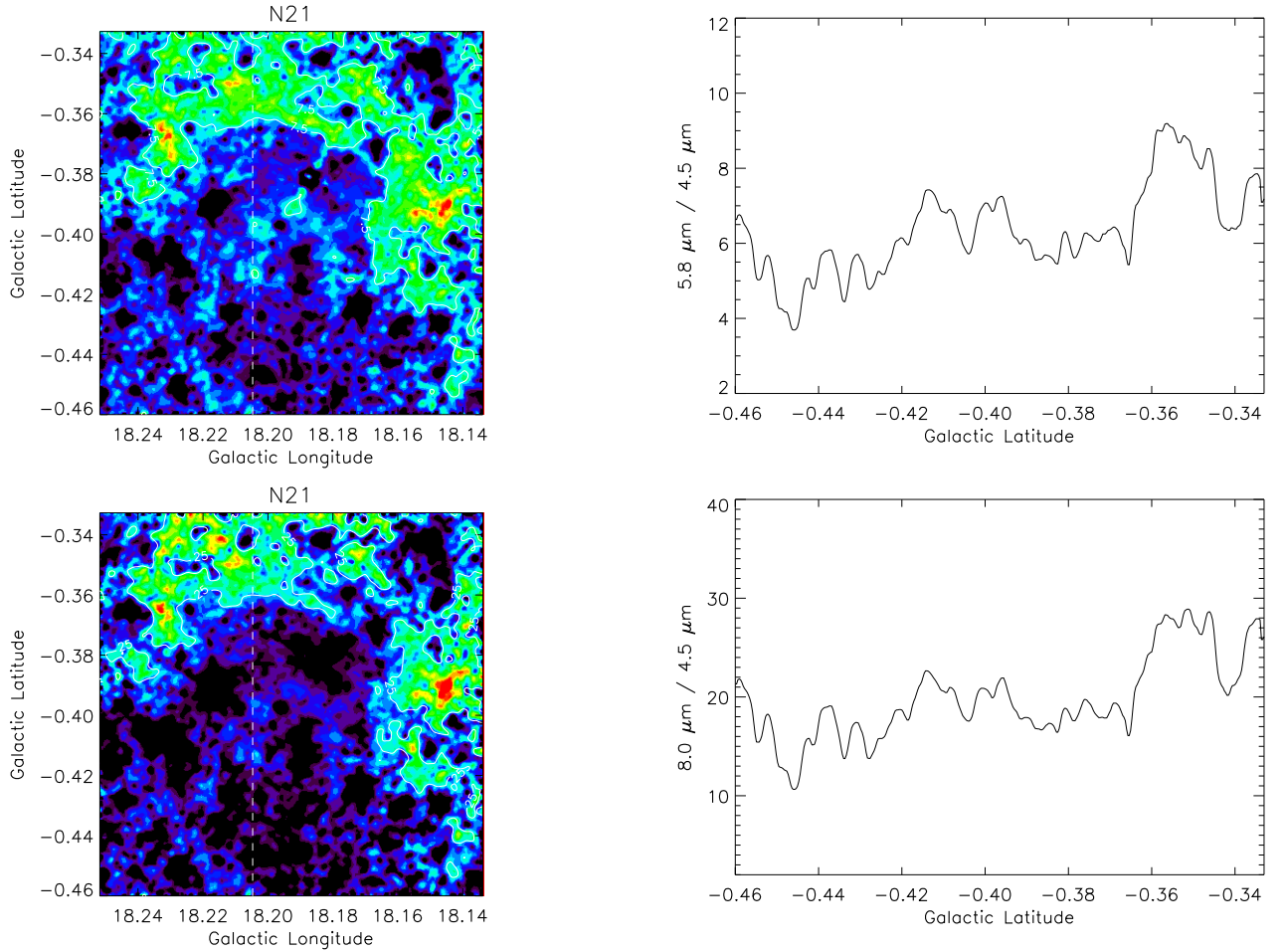


Fig. 11.— N49: PAH destruction as measured from $5.8 \mu\text{m} / 4.5 \mu\text{m}$ (upper-left) and $8.0 \mu\text{m} / 4.5 \mu\text{m}$ (lower-left). The color scale ranges from 7 to 13 (upper-left, blue-to-red) and 15 to 42 (lower-left, blue-to-red). The contours represent ratios of 8.5 (upper-left) and 28 (lower-left). Longitude slices at constant latitude (upper-right and lower-right). Dashed white lines at left indicate position of slices show at right.

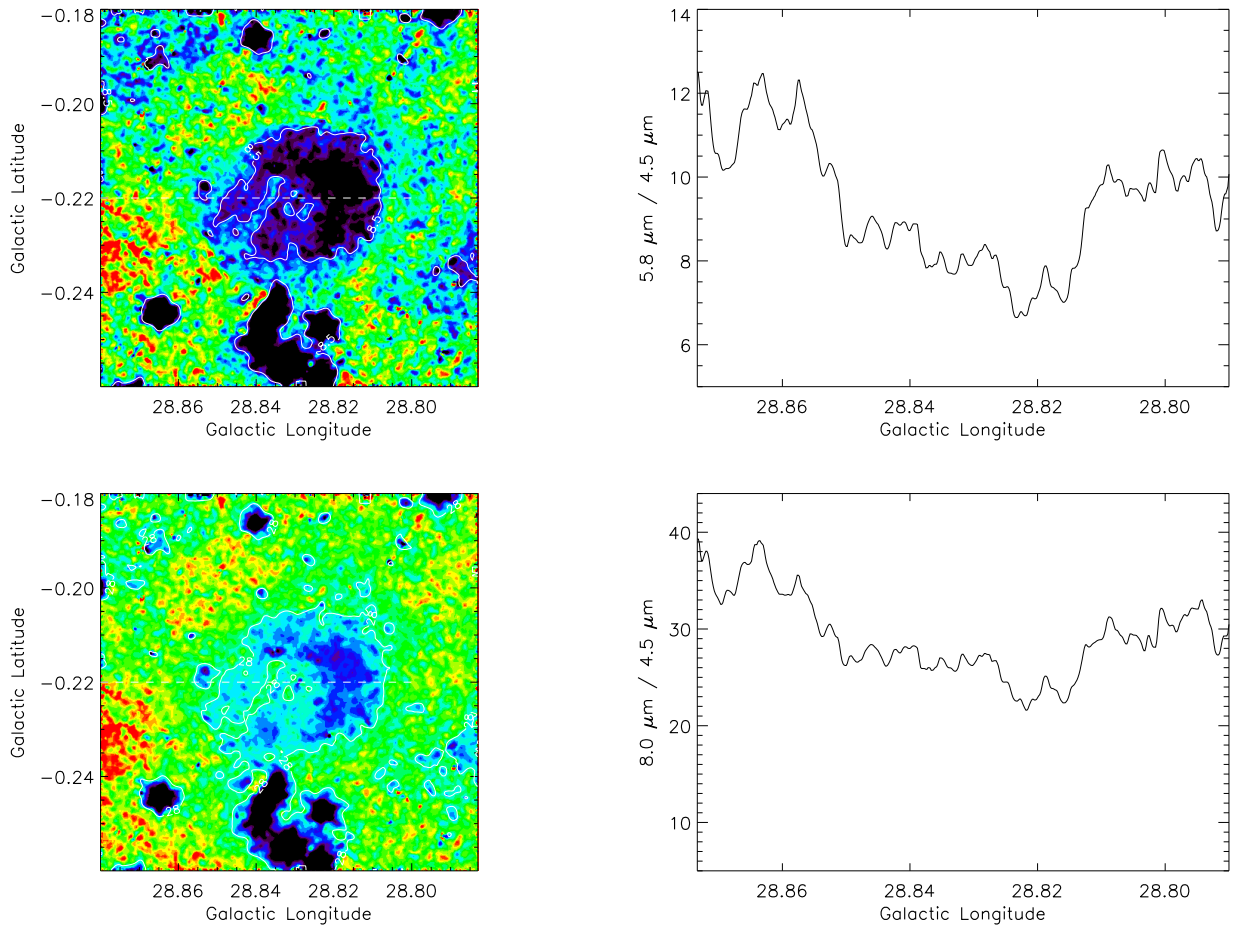
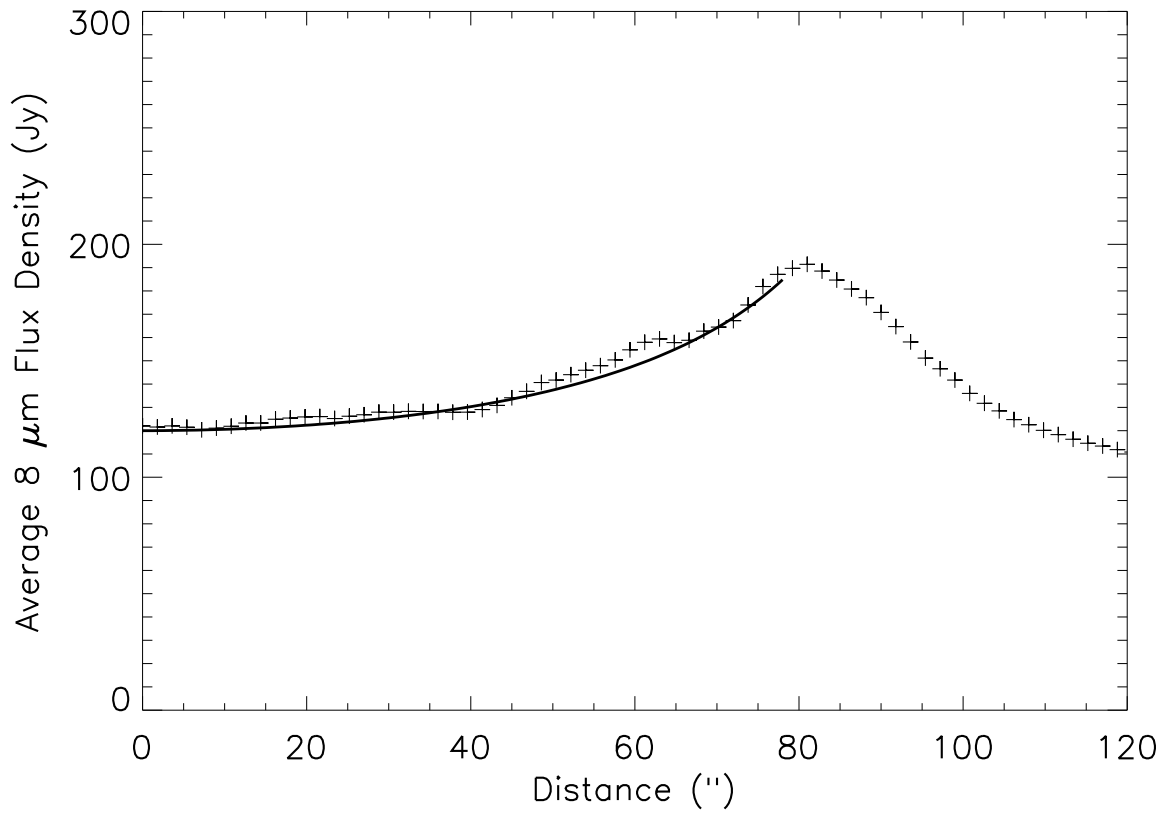


Fig. 12.— N49: Observed, azimuthally averaged, radial profile of $8\ \mu\text{m}$ emission (+) compared with a model of shell emission (solid line) normalized to the observed brightness at the center of N49.



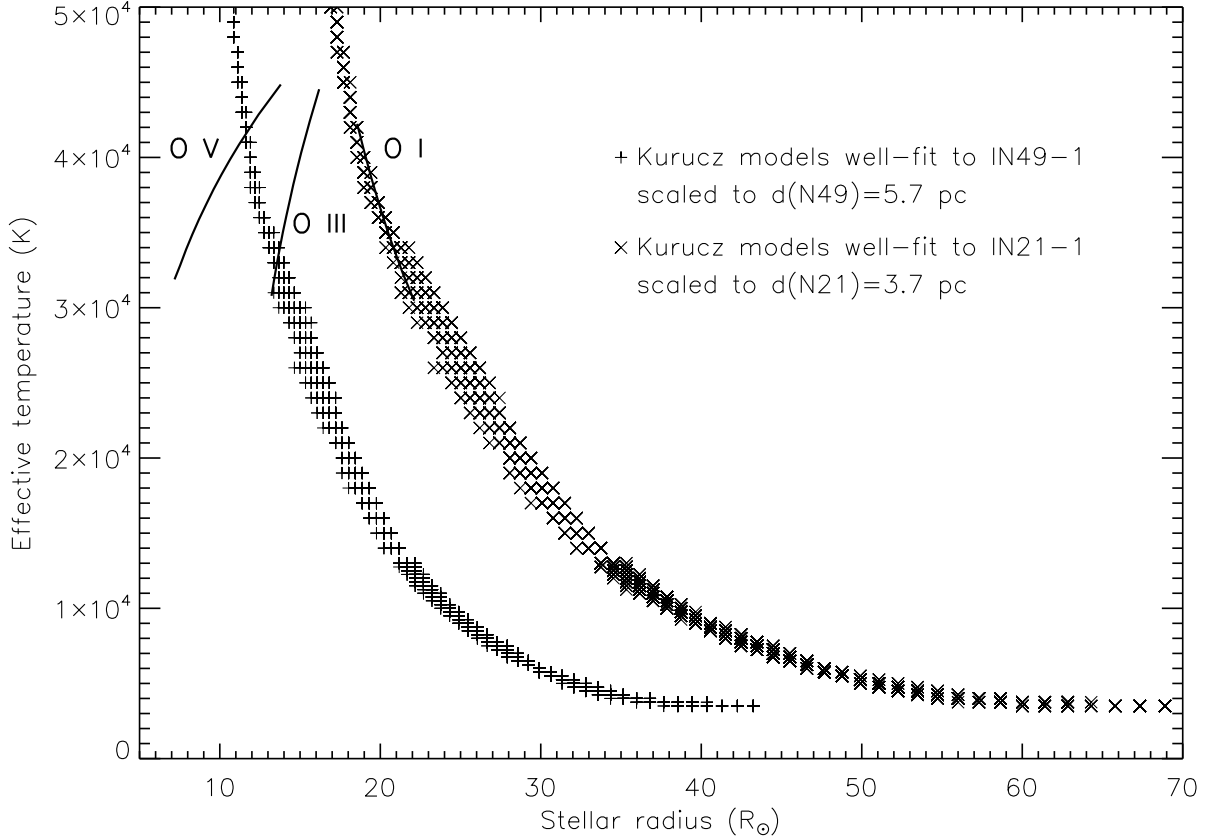


Fig. 13.— Examples of spectral type determinations for candidate ionizing stars. The set of well-fit Kurucz (1993) stellar atmosphere models to the NIR–MIR SEDs of the best candidate ionizing stars in N49 and N21 have been plotted in $T_{\text{eff}}-R$ space, where R is calculated by scaling the model fits to the distance of their respective bubbles. The O-star $T_{\text{eff}}-R$ relations of Martins et al. (2005) are overplotted as heavy curves for dwarfs, giants, and supergiants. The curves extend from types O3 to O9.5 for each luminosity class. From the intersections of the curves with the loci of model fits, a spectral type of O5 V or late O III is consistent with the observed fluxes of IN49-1. The spectral type of IN21-1 is degenerate among O supergiants. These degeneracies in spectral type can be lifted by considering the ionizing flux required to produce the H II regions in which the stars are located.

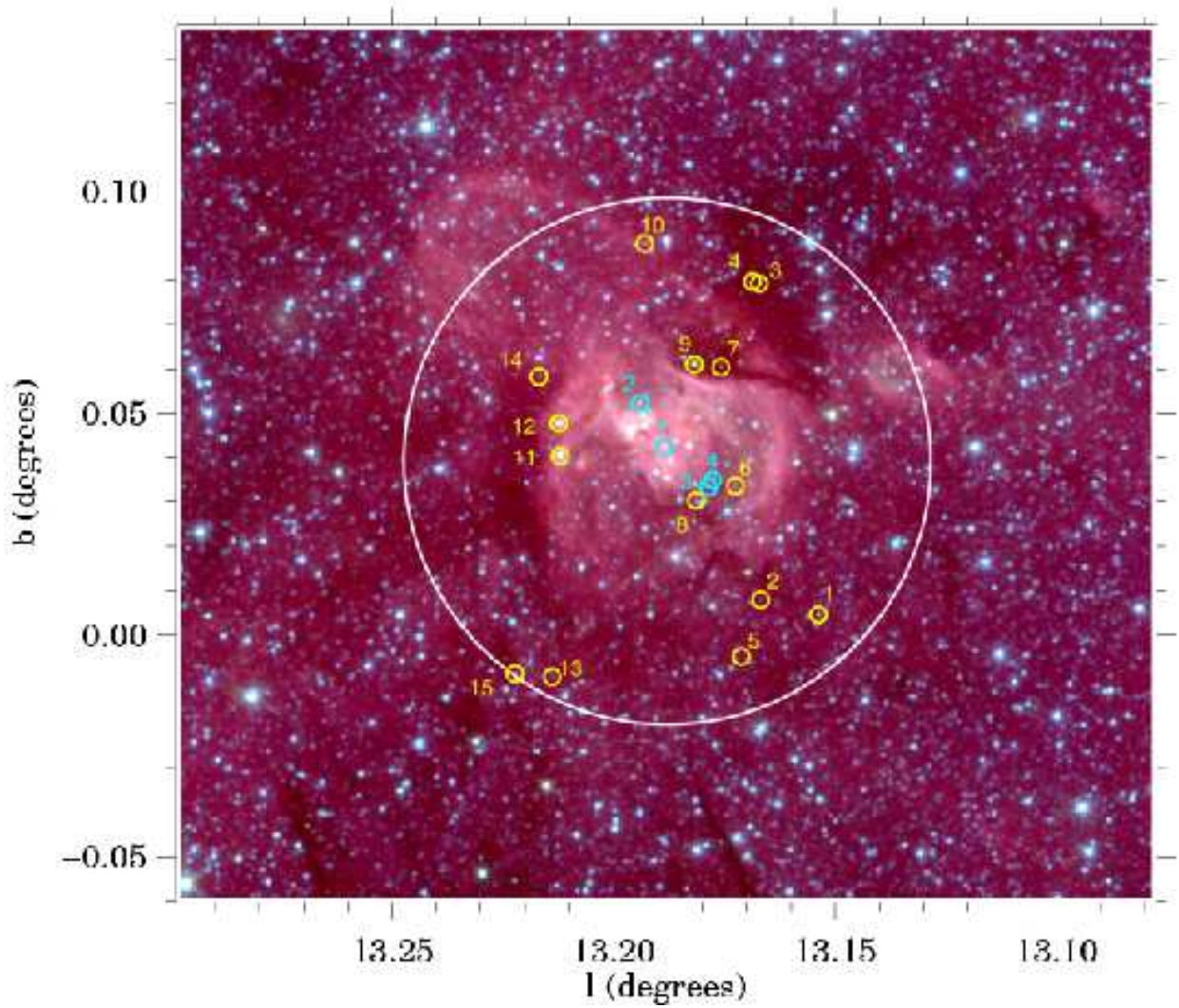


Fig. 14.— N10 image in $3.6 \mu\text{m}$ (blue), $4.5 \mu\text{m}$ (green) and $8.0 \mu\text{m}$ (red). Positions of YSO candidates in Table 1 and candidate ionizing stars in Table 2 are marked with yellow and cyan circles, respectively. The large white circle shows the area in which the GLIMPSE Point Source Archive was searched for YSO candidates.

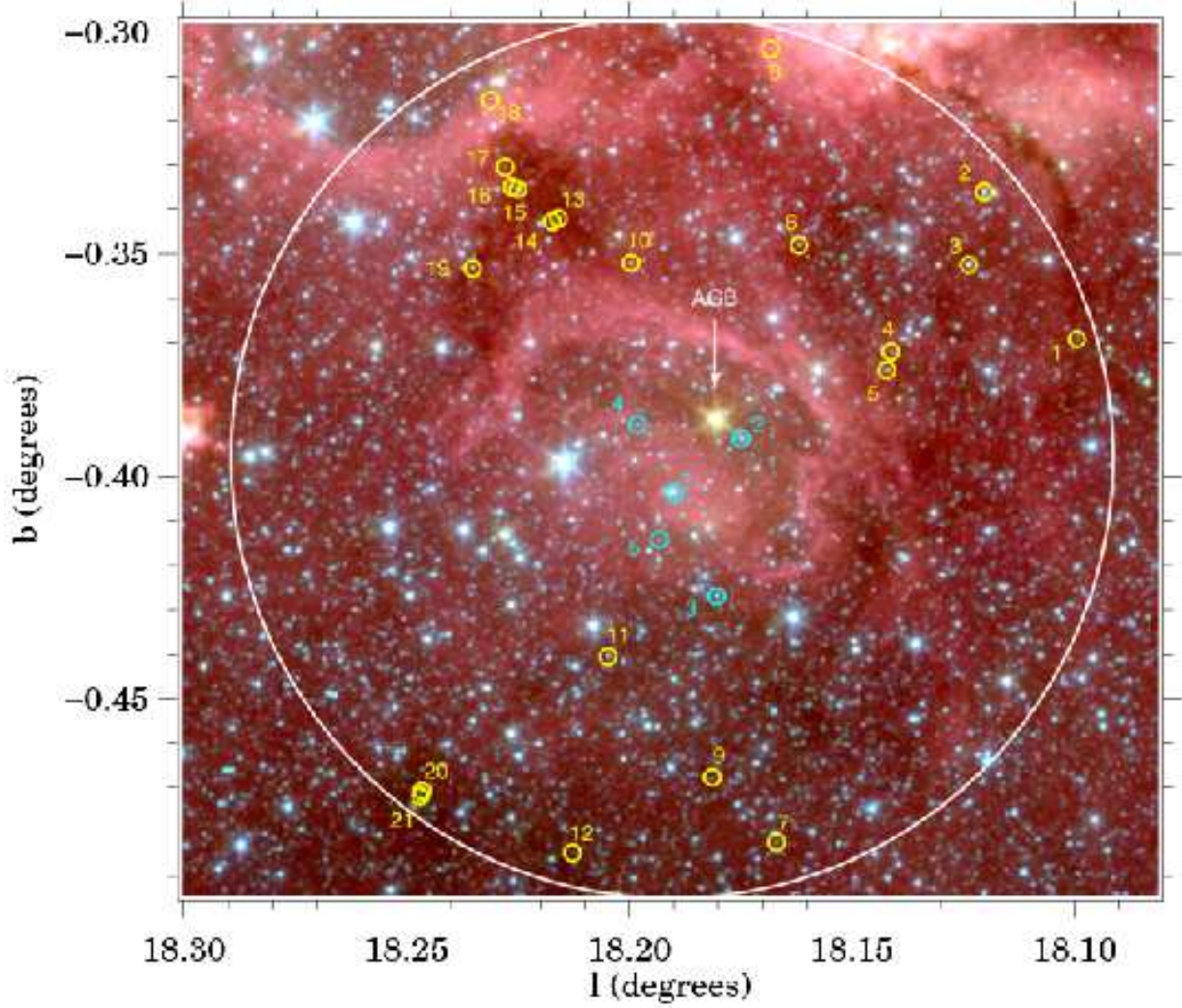


Fig. 15.— Same as Fig. 14, but showing bubble N21. The MIR-bright asymptotic giant branch star is labeled. Although this star appears to lie inside the bubble, it is most likely a background AGB star.

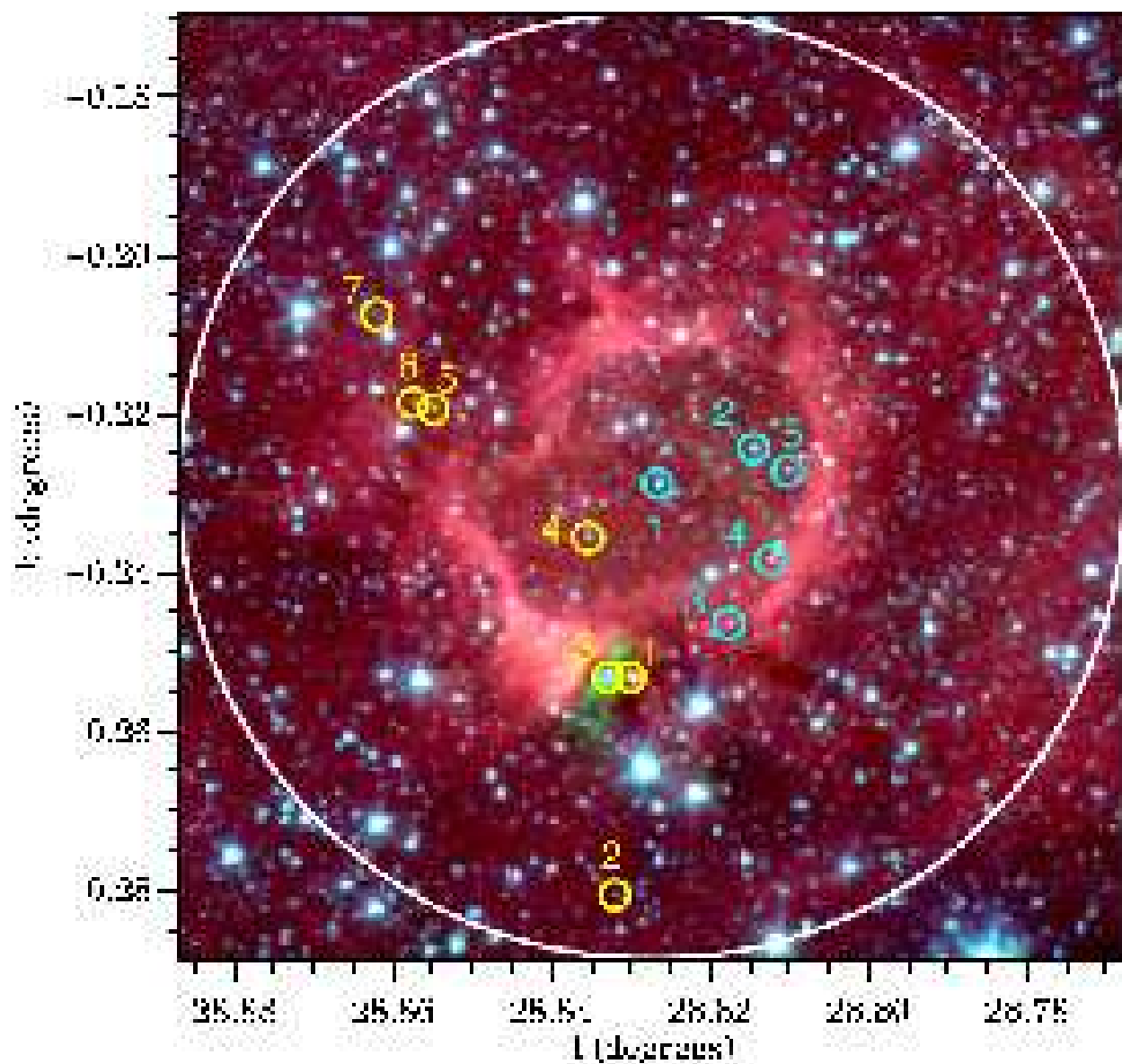


Fig. 16.— Same as Fig. 14, but showing bubble N49.

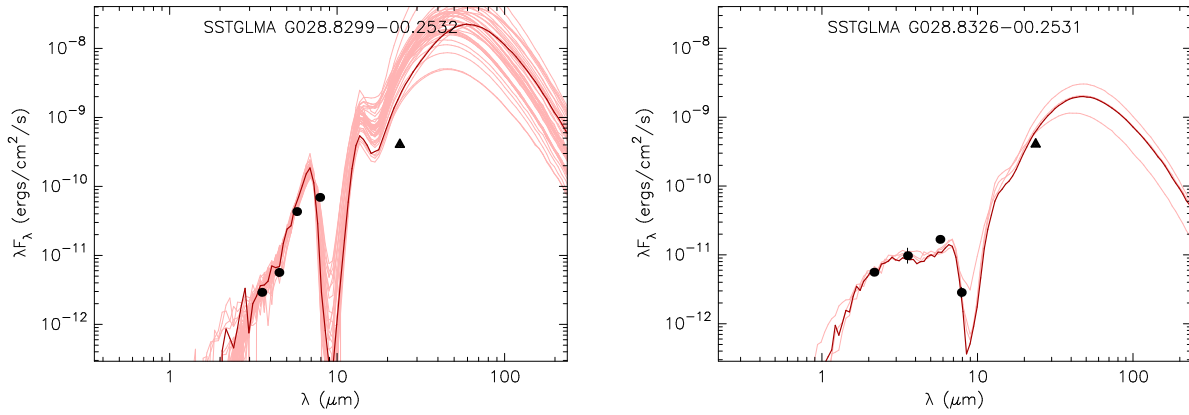


Fig. 17.— Model fits to the SEDs of 2 candidate massive YSOs appearing on the rim of bubble N49. Measured broadband fluxes and lower limits are plotted as heavy dots with error bars and triangles, respectively. The set of well-fit model SEDs are overplotted as curves, with the heavy curve showing the best fit. *Left panel:* YSO N49-1 is extremely red in the GLIMPSE bands. *Right panel:* YSO N49-3 is associated with the brightest extended $4.5 \mu\text{m}$ emission in our sample, indicative of a powerful molecular outflow. Because the $4.5 \mu\text{m}$ emission is extended, and the YSO models do not incorporate molecular line emission, this band was not used in fitting the SED of this object. These sources are very close together, and their $24 \mu\text{m}$ emission is borderline confused and saturated, so lower limits were employed for the fitting.

Table 1. Model Parameters for YSO Candidates Associated with the Bubbles

ID	Name (<i>Gl + b</i>)	N_{fits}	M_* (M_{\odot})			L_{TOT} (L_{\odot})			\dot{M}_{env} ($M_{\odot} \text{ yr}^{-1}$)			Stage	Comments ^a
			best	min	max	best	min	max	best	min	max		
N10-1	G013.1536+00.0040	86	.7	2.9	7.3	315	76	532	2.3E-04	4.1E-05	9.4E-04	I	
N10-2	G013.1667+00.0074	12	.1	1.0	5.5	26	15	682	1.5E-04	0.0E+00	4.1E-04	I	
N10-3	G013.1670+00.0794	7	.6	0.9	3.0	43	33	128	3.3E-04	2.1E-04	4.1E-04	I	IRDC
N10-4	G013.1686+00.0798	3	1.7	3.7	3.7	107	107	107	2.1E-04	2.1E-04	2.1E-04	I	IRDC
N10-5	G013.1711-00.0055	351	3.4	0.3	7.1	35	9	766	0.0E+00	0.0E+00	3.8E-04	II	
N10-6	G013.1725+00.0333	597	.1	0.7	7.5	152	12	600	2.2E-05	1.6E-06	6.0E-04	I	Bub
N10-7	G013.1758+00.0604	57	.4	5.8	16.7	6479	273	8570	8.9E-04	2.2E-04	1.6E-03	I	Rim, IRDC
N10-8	G013.1814+00.0300	2395	3.6	0.9	11.1	246	24	3225	0.0E+00	0.0E+00	1.4E-03	I	Bub
N10-9	G013.1818+00.0610	197	.3	0.4	13.5	2820	142	13880	1.0E-03	3.7E-06	2.1E-03	I	Rim, IRDC, [4.5]
N10-10	G013.1931+00.0885	84	5.1	1.9	6.2	440	62	440	2.2E-03	2.2E-05	2.2E-03	I	PDR
N10-11	G013.2124+00.0401	42	0.7	8.4	12.7	3858	2170	6900	9.3E-04	1.5E-04	1.0E-03	I	Rim
N10-12	G013.2127+00.0476	244	8.9	8.9	17.1	5505	3342	29590	2.2E-04	6.4E-05	5.8E-03	I	Rim
N10-13	G013.2142-00.0101	27	3.6	2.5	4.2	206	44	258	0.0E+00	0.0E+00	0.0E+00	II	
N10-14	G013.2172+00.0582	2400	4.2	1.4	8.7	144	33	1349	0.0E+00	0.0E+00	4.6E-04	I	IRDC
N10-15	G013.2227-00.0093	13	0.5	0.2	0.5	16	15	20	2.9E-06	2.3E-06	3.9E-06	I	IRDC
N21-1	G018.0981-00.3692	1302	.8	0.4	4.6	27	6	87	1.3E-05	1.2E-06	2.3E-04	I	IRDC
N21-2	G018.1192-00.3359	2212	.3	3.2	6.9	314	78	1563	0.0E+00	0.0E+00	4.3E-05	II	PDR
N21-3	G018.1227-00.3524	49	.4	4.6	6.8	1151	383	1543	0.0E+00	0.0E+00	0.0E+00	II	PDR
N21-4	G018.1403-00.3721	1581	.5	1.5	8.6	102	30	1216	0.0E+00	0.0E+00	5.4E-04	I	PDR
N21-5	G018.1412-00.3763	1166	.9	2.6	5.8	163	76	719	0.0E+00	0.0E+00	1.4E-04	II	PDR
N21-6	G018.1611-00.3480	354	.1	2.6	4.2	80	42	141	0.0E+00	0.0E+00	1.3E-07	II	PDR
N21-7	G018.1662-00.4833	799	.6	1.6	4.0	44	16	197	0.0E+00	0.0E+00	1.1E-08	II	
N21-8	G018.1677-00.3034	60	.5	1.2	8.0	474	35	903	5.0E-05	1.0E-05	2.9E-04	I	PDR
N21-9	G018.1808-00.4686	3546	.8	0.5	4.7	58	8	140	0.0E+00	0.0E+00	2.3E-04	I	
N21-10	G018.1992-00.3520	276	4.2	3.2	5.2	258	144	583	0.0E+00	0.0E+00	0.0E+00	II	PDR
N21-11	G018.2044-00.4412	1015	2.9	0.9	5.1	59	26	143	0.0E+00	0.0E+00	3.4E-04	I	
N21-12	G018.2125-00.4857	25	1.0	0.5	2.0	11	7	37	2.4E-05	6.8E-06	4.7E-04	I	
N21-13	G018.2157-00.3419	33	8.6	1.2	8.6	1443	62	1735	1.3E-03	1.2E-05	1.3E-03	I	IRDC
N21-14	G018.2171-00.3426	83	0.5	0.2	6.4	16	16	379	2.9E-06	2.3E-06	1.3E-03	I	IRDC
N21-15	G018.2249-00.3352	371	6.1	1.1	6.1	358	19	358	6.4E-05	0.0E+00	5.8E-04	I	IRDC
N21-16	G018.2262-00.3348	63	1.3	0.4	2.4	44	34	134	6.7E-06	4.3E-06	3.7E-05	I	IRDC
N21-17	G018.2277-00.3303	3136	1.5	0.7	5.2	69	12	154	0.0E+00	0.0E+00	3.0E-04	I	IRDC
N21-18	G018.2311-00.3150	5360	1.7	0.7	5.7	18	10	546	0.0E+00	0.0E+00	2.9E-04	I	PDR
N21-19	G018.2351-00.3532	83	5.1	0.4	6.0	182	26	480	9.4E-04	0.0E+00	9.4E-04	I	IRDC
N21-20	G018.2466-00.4717	20	2.9	1.2	4.1	139	56	235	1.3E-03	0.0E+00	1.3E-03	I	
N21-21	G018.2470-00.4728	19	5.5	2.0	6.0	161	46	194	6.3E-04	1.5E-04	9.9E-04	I	
N49-1	G028.8299-00.2532	47	9.0	14.0	29.0	30040	5251	102400	8.9E-04	4.1E-04	6.7E-03	I	Rim, IRDC
N49-2	G028.8318-00.2808	1461	34.0	1.6	4.7	60	19	205	0.0E+00	0.0E+00	1.7E-05	II	
N49-3	G028.8326-00.2531	4	0.5	9.3	12.7	2942	2288	3657	3.4E-04	1.2E-04	3.4E-04	I	Rim, IRDC,[4.5]
N49-4	G028.8352-00.2354	1578	33.7	2.8	7.9	207	101	1050	0.0E+00	0.0E+00	7.0E-04	I	Bub
N49-5	G028.8547-00.2192	72	1.3	0.3	8.1	44	34	924	6.7E-06	4.0E-06	1.0E-03	I	PDR
N49-6	G028.8573-00.2184	276	0.5	0.2	6.9	16	15	379	2.9E-06	2.3E-06	1.2E-03	I	PDR
N49-7	G028.8619-00.2072	812	2.3	0.7	3.9	18	7	35	1.2E-06	8.6E-08	9.3E-05	I	

^aThe flags in the comments column are as follows: Rim=source on the rim of the bubble; IRDC=source within an infrared dark cloud; PDR=source within bright diffuse PAH background emission in the photodissociation region; and [4.5]=source exhibits extended excess emission at 4.5 μm .

Table 2. Candidate Ionizing Stars

ID	Name ($Gl + b$)	Spectral Type	A_V	Best?
IN10-1	13.1887+00.0421	O7.5 V	7	✓
IN10-2	13.1942+00.0521	O6.5 V	7	
IN10-3	13.1786+00.0331	O6 V	5	✓
IN10-4	13.1777+00.0346	O7 V	8	
IN21-1	18.1893-00.4041	early B I ^a	6	✓
IN21-2	18.1742-00.3918	O6 V	9	
IN21-3	18.1798-00.4275	O8 V	7.5	
IN21-4	18.1977-00.3886	O8.5 V	13	
IN21-5	19.1928-00.4147	early B V	8	
IN49-1	28.8263-00.2287	O5 V	10.5	✓
IN49-2	28.8142-00.2241	O5.5 V	7.5	
IN49-3	28.8174-00.2464	O7 V	7.5	
IN49-4	28.8119-00.2383	O9	10	
IN49-5	28.8098-00.2270	B0	6	

^aFor this star, the observed $T_{\text{eff}}-R$ relation at the 3.7-kpc kinematic distance of N21 overlaps with the MSH05 curve for O supergiants, so the spectral type is degenerate. We have assigned a spectral type based upon the Lyman continuum photon flux required to ionize the H II region in N21.

